

# Performance of sCO<sub>2</sub> coal-fired power plants at various power capacities

Zhaofu Wang<sup>a</sup>, Jinliang Xu<sup>a,b,\*</sup>, Tianze Wang<sup>a</sup>, Zheng Miao<sup>a,b</sup>, Qingyang Wang<sup>a,b</sup>,  
Guanglin Liu<sup>a,b</sup>

<sup>a</sup> Beijing Key Laboratory of Multiphase Flow and Heat Transfer for Low Grade Energy Utilization, North China Electric Power University, Beijing, 102206, China

<sup>b</sup> Key Laboratory of Power Station Energy Transfer Conversion and System (North China Electric Power University), Ministry of Education, Beijing, 102206, China

## ARTICLE INFO

Handling Editor: Jin-Kuk Kim

### Keywords:

sCO<sub>2</sub> cycle  
Coal-fired power plant  
Comprehensive model  
Optimum efficiency

## ABSTRACT

Herein, the effect of the power capacity,  $W_{net}$ , on the performance of supercritical carbon dioxide (sCO<sub>2</sub>) coal-fired power plants is investigated, with  $W_{net}$  in the range of (100–1000) MWe. A comprehensive model was established wherein the sCO<sub>2</sub> cycle was coupled with the models of various components. For the sCO<sub>2</sub> boiler, the total thermal load was assigned to various heaters, and the pressure drop in each heater was calculated. Owing to the strong penalty effect of the pressure drop, both total flow mode (TFM) and partial flow mode (PFM) were applied to the sCO<sub>2</sub> boiler. A fluid network integrating the recuperator units was established for heat recovery in the system. A thermal-hydraulic model was proposed for a single unit and an integration package. Various losses were considered in the prediction of the efficiencies of axial flow turbines and compressors. The thermal efficiency increases, attains a maximum, and then decreases with increase of  $W_{net}$ . This parabolic distribution results from the tradeoff between the decreased efficiency owing to pressure drops in the heat exchangers and the increased efficiency of the turbomachinery. The maximum thermal efficiency occurred at  $W_{net}$  of 300 MWe and 200 MWe when using the PFM and TFM, respectively. Based on the results, PFM is found to eliminate the penalty effect of pressure drops. Our study provides guidelines for the design and operation of sCO<sub>2</sub> coal-fired power plants.

## 1. Introduction

To achieve carbon neutrality by 2060, the utilization of fossil energy has reduced and the utilization of renewable energy has increased in China (Xu et al., 2020; Qi et al., 2023). Because renewable energy is unstable owing to its oscillating and intermittent characteristics (Xie et al., 2023), fossil energy such as coal shall still be used for power generation in several decades (National Bureau of Statistics of China, 2020), which shall not only maintain high thermal efficiency, but also be quick response to external load variations (Meng et al., 2022). Compared with the water-steam Rankine cycle power generation system, supercritical carbon dioxide (sCO<sub>2</sub>) coal-fired power generation exhibits a higher thermal efficiency and faster load regulation rate (Dostal, 2004; Liu et al., 2020a; Xu et al., 2019). Available studies on sCO<sub>2</sub> coal-fired power generation systems have focused on rated power capacity of 1000 MWe (Moulec, 2013; Xu et al., 2018; Yang et al., 2020; Liu et al., 2020b; Li et al., 2019a). The objective of the present study was to explore the performance of sCO<sub>2</sub> power generation system at various power capacities in the range of (100–1000) MWe.

Initially, Moulec (2013) and Mecheri et al. (Mecheri and Moulec, 2016) presented a design for a 1000 MWe sCO<sub>2</sub> coal-fired power plant and evaluated its economic performance. A fraction of the sCO<sub>2</sub> stream was extracted from a low-temperature recuperator to absorb residual heat at tail flue, resulting in higher thermal efficiency than water-steam Rankine cycle system. Park et al. (2018) proposed a simpler sCO<sub>2</sub> Brayton cycle, showing better performance than the Moulec's cycle. Collaborating with Babcock & Wilcox (B&W), Electric Power Research Institute (EPRI) highlighted the difficulties in developing sCO<sub>2</sub> boilers for sCO<sub>2</sub> power plants (Thimsen and Weitzel, 2016). They provided a design for a small-scale sCO<sub>2</sub> boiler. Xi'an Thermal Power Research Institute (TPRI) has been developing a 5 MWe sCO<sub>2</sub> power generation system driven by natural gas boiler (Li et al., 2019b). The demonstration of key components and the whole system have been completed (Wang et al., 2018; Han et al., 2019).

To achieve a high thermal efficiency, Xu et al. (2018) conducted fundamental investigations on an sCO<sub>2</sub> coal-fired power plant; the key issues in the applications are discussed in Ref. (Xu et al., 2018). A challenge exists in the recovery of flue gas energy in a wide temperature

\* Corresponding author. North China Electric Power University, 2 Beinong Rd, Changping District, Beijing, China.

E-mail address: [xjl@ncepu.edu.cn](mailto:xjl@ncepu.edu.cn) (J. Xu).

<https://doi.org/10.1016/j.jclepro.2023.137949>

Received 14 April 2023; Received in revised form 24 June 2023; Accepted 28 June 2023

Available online 29 June 2023

0959-6526/© 2023 Elsevier Ltd. All rights reserved.

range of (1500–1200) °C. Cascade energy utilization was proposed to solve this issue (Sun et al., 2018) wherein the top cycle, bottom cycle, and air preheater absorbed high-temperature, moderate-temperature, and low-temperature flue gas energies, respectively. Because the top and bottom cycles operate in different temperature zones, an efficiency gap exists owing to the lower efficiency of the bottom cycle. The overlapping energy utilization strategy sets an overlap zone in the high-temperature region, and the flue gas energy in this region is absorbed by both cycles, instead of only the top cycle (Sun et al., 2019). Pressure drop penalty is another issue to be resolved (Xu et al., 2018). A partial flow strategy was proposed to reduce the flow rate and flow length of each module to half those of a conventional module. Therefore, the partial flow strategy generates a series of modules across the entire sCO<sub>2</sub> boiler so that the pressure drop of the sCO<sub>2</sub> boiler is decreased to a level similar to that of a water-steam boiler (Xu et al., 2018). Progress has been made in system design and analysis (Sun et al., 2020; Xu et al., 2021; Guo et al., 2020; Wang et al., 2021a, 2022), basic understanding of energy conversion mechanisms (Zhu et al., 2019, 2020; Wang et al., 2021b), and development of various components such as sCO<sub>2</sub> boilers, heat exchanger, turbines, and compressors (Liu et al., 2022; Zhou et al., 2020; Li et al., 2022; Wang et al., 2023).

The studies have focused on sCO<sub>2</sub> coal-fired power systems with a rated power capacity of 1000 MWe. Xu et al. (Liu et al., 2020c) developed scale laws regarding the variations in performance parameters at various power capacities. Owing to the enhanced penalty effect of pressure drops at larger power capacities, the thermal efficiency of the system decreases as the power capacity increases. To mitigate the penalty effect of the pressure drops, the partial flow mode (PFM), which is essential for power generation systems with capacities greater than 100 MWe, was introduced. The PFM is not required for a power capacity less than 100 MWe. The work presented in Ref. (Liu et al., 2020c) considered the effect of pressure drops on the system performance, with other parameters such as the isentropic efficiencies of turbines and compressors fixed at different power capacities.

In contrary to Ref. (Liu et al., 2020c), the present study considers various factors affecting system performance, including the varied efficiencies of turbines and compressors and the thermal hydraulic characteristics of printed circuit heat exchangers (PCHE) at different power capacities. CO<sub>2</sub> leakage, which is severe for small-scale radial turbomachinery, is mitigated when using large-scale axial turbomachinery (Xu et al., 2019; Cho et al., 2018); The PCHE is a better choice for the sCO<sub>2</sub> cycle. However, owing to the limited thermal load supplied by a single PCHE (Jiang et al., 2018a), a fluid network integrating several PCHE units was established to fill the gap between the load required for heat recovery in the sCO<sub>2</sub> cycle and maximum load supplied by a single PCHE.

The originality of this study is presented as follows: (i) A comprehensive model of an sCO<sub>2</sub> coal-fired power plant was established, focusing on the effect of power capacities on system performance. Previous studies seldom considered the coupling of the sCO<sub>2</sub> cycle and various components at power capacities in the range of (100–1000) MWe (Liu et al., 2020b; Mecheri and Moullec, 2016; Park et al., 2018). Most studies fixed the turbine and compressor efficiencies as constants at specific power capacities (Mecheri and Moullec, 2016; Liu et al., 2020c). (ii) A fluid network integrating recuperator unit was established for heat recovery of the sCO<sub>2</sub> power system, and a thermal-hydraulic model was proposed for a single unit and integration package. (iii) With a continuous increase in the power capacity ( $W_{net}$ ) from 100 MWe to 1000 MWe, the thermal efficiency increased, attained a maximum, and then decreased. This parabolic distribution is caused by the tradeoff between negative and positive effects, the former referring to the decreased efficiency on increasing  $W_{net}$  owing to pressure drops in the heat exchangers and the latter referring to the increased efficiency on increasing  $W_{net}$  owing to the isentropic efficiency of the turbomachinery. The remainder of this paper is organized as follows. The layout of the sCO<sub>2</sub> coal-fired system is described in Section 2. The numerical

model is described in Section 3, which includes computations for the cycle, boiler, PCHE, turbine, and compressor. The results and discussion are presented in Section 4, and the conclusions are summarized in Section 5.

## 2. sCO<sub>2</sub> coal-fired power generation system

Fig. 1 shows the sCO<sub>2</sub> cycle used in this study, which incorporates the top and bottom cycles, component sharing, and overlap energy utilization (Sun et al., 2019). The top and bottom cycles are represented by the black and blue lines, respectively. Both cycles use RC + RH, where RC and RH represent the recompression cycle and reheating, respectively. They absorb flue gas energies in the high-temperature zone, represented by Heater 1, and in the moderate-temperature zone, represented by Heater 2. Heater 4b is in the high-temperature flue gas zone, which is included in the bottom cycle to increase its efficiency; therefore, overlap energy utilization is fulfilled. Because several facilities in the two cycles share identical pressure and temperature parameters, the two cycles are combined, which is referred to as component sharing in Ref. (Sun et al., 2019). C1 and C2 represent the two compressors, while high-temperature recuperator (HTR), HTR2, and low-temperature recuperator (LTR) represent the internal heat exchangers used for heat recovery. The cooler dissipates additional heat from the entire system to the environment. The assumptions made in the cycle computation are as follows:

- Steady operation of the sCO<sub>2</sub> coal-fired power system is considered.
- Physical properties of sCO<sub>2</sub> are computed by the commercial software NIST.
- A fluid network was involved in the sCO<sub>2</sub> cycle; the mass flow rates, pressure drops, and thermal loads were balanced in various components of the system, ensuring that the temperature difference did not exist at any mixing point. Therefore, exergy destruction owing to the mixing did not occur.
- In heat exchangers, the pinch temperature refers to the minimum temperature difference in the  $T$ - $Q$  curve, where  $T$  and  $Q$  represent the temperature and thermal load, respectively. Because the heat recovery reaches three to four times the net power output of the sCO<sub>2</sub> cycle, the pinch temperature influences the cycle performance. For recuperator heat exchangers of LTR and HTR in Fig. 1, the pinch temperature is set as 10 °C (Table 1) (Dostal, 2004; Mecheri and Moullec, 2016). A very low pinch temperature significantly increases the cost of heat exchangers, whereas a very high pinch temperature deteriorates the cycle efficiency (Xu et al., 2021; Qiao et al., 2020). Therefore, the pinch temperature of 10 °C is suitable.
- Owing to the gas state of tail flue and smaller heat transfer coefficient, the pinch temperature is set as 30 °C (Table 1) for air preheater and Heater 4a in Fig. 1 (Sun et al., 2018).
- The main vapor parameters at the inlet of turbine T1 are 620 °C/30 MPa at the power capacities in the range of (100–1000) MWe. This is referenced to commercial water-steam Rankine cycle (Fan et al., 2018), and the sCO<sub>2</sub> power cycle also operates well in this range considering the temperature and pressure that can be sustained by the materials adapting to sCO<sub>2</sub> (Holcomb et al., 2016).
- The main vapor parameters at the inlet of compressor C1 are 32 °C/7.6 MPa, from Refs. (Dostal, 2004; Li et al., 2020). For the operation of the compressor, selecting an inlet pressure approaching the critical pressure of 7.377 MPa, where the power consumption of the compressor can be minimized, is appropriate. A pressure that is too low may experience a critical point that deteriorates the compressor performance owing to the condensed droplets in the compressor. Therefore, a pressure of 7.6 MPa was suitable. The extra heat in the system was dissipated by the cooler. Considering that the sCO<sub>2</sub> stream was cooled by water at temperature of 20 °C, a temperature of 32 °C at the compressor inlet was reasonable.

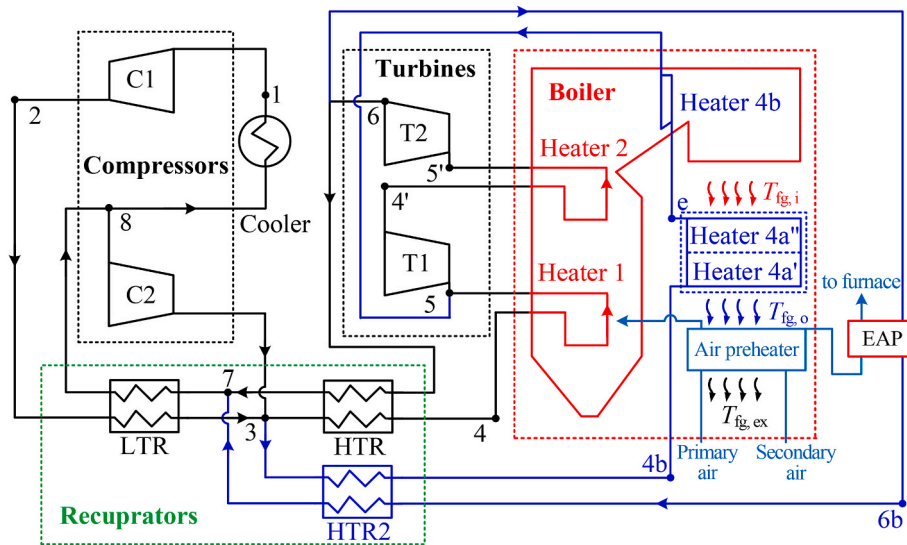


Fig. 1. The layout of sCO<sub>2</sub> coal-fired power plant (Liu et al., 2020c).

### 3. Numerical model

In our previous study, we analyzed the pressure drop penalty of an sCO<sub>2</sub> boiler on the cycle performance at various power capacities (Liu et al., 2020c). In contrast we herein present a comprehensive investigation of the power plant performance at different power capacities. The cycle analysis, represented by the cycle subroutine, is coupled with the models of components, including the sCO<sub>2</sub> boiler, recuperator heat exchangers, axial turbines, and axial compressors, represented by the three subroutines of components (Fig. 2). The four types of components are heat exchangers for the sCO<sub>2</sub> boiler and recuperators and thermal-power conversion machines for the turbines and compressors. Therefore, the cycle computation requires two levels of iteration; the first level refers to the iteration of the pressure drops in the sCO<sub>2</sub> boiler and recuperators, whereas the second level refers to the iteration of the turbine and compressor efficiencies. The entire computation is assumed to converge until the pressure drops in various heat exchangers and axial turbomachinery efficiencies converge. The entire cycle consists of a complicated fluid network. The mass flow rates, pressure drops, and thermal loads should be balanced across the various components of the entire system.

#### 3.1. Computation of sCO<sub>2</sub> cycle

The flue gas energy is divided into three regions: high-temperature, moderate-temperature, and low-temperature. The heat balance equations for each region are as follows:

$$\begin{cases} \varphi B_{\text{cal}}(h_{\text{flame}} - h_{\text{fg},i}) = Q_{\text{Heater1}} + Q_{\text{Heater2}} + Q_{\text{Heater4b}} \\ \varphi B_{\text{cal}}(h_{\text{fg},i} - h_{\text{fg},o}) = Q_{\text{Heater4a}} \\ \varphi B_{\text{cal}}(h_{\text{fg},i} - h_{\text{fg},\text{ex}}) = Q_{\text{AP}} \end{cases} \quad (1)$$

here,  $h$  represents the enthalpy of flue gas, and the subscripts  $\text{fg},i$ ,  $\text{fg},o$ , and  $\text{fg},\text{ex}$  represent the interface temperatures between the three temperature zones of flue gas,  $\varphi$  denotes the insulation coefficient of the boiler, and  $B_{\text{cal}}$  represents the coal consumption rate. The high-temperature flue gas heat is absorbed by Heaters 1, 2, and 4b, whereas moderate-temperature flue gas heat is absorbed by Heaters 4a and 4a'. The low-temperature flue gas heat is absorbed by an air preheater.

The thermal efficiency  $\eta_{\text{th}}$  of the cycle is calculated as

$$\eta_{\text{th}} = \frac{W_{\text{net}}}{Q_{\text{total}}} \quad (2)$$

where  $W_{\text{net}}$  is the power capacity, which is in the range of (100–1000) MWe. The total heat absorption of the sCO<sub>2</sub> cycle can be expressed as follows:

$$Q_{\text{total}} = Q_{\text{Heater 1}} + Q_{\text{Heater 2}} + Q_{\text{Heater 4b}} + Q_{\text{Heater 4a}} + Q_{\text{AP}} - Q_{\text{EAP}} \quad (3)$$

The chemical exergy of coal is equal to the input exergy of the system  $E_{\text{in}}$  (Fu, 2005).

$$E_{\text{in}} = m_{\text{coal}} Q_{\text{LHV}} \left( 1.0064 + 0.1519 \frac{H_{\text{ar}}}{C_{\text{ar}}} + 0.0616 \frac{O_{\text{ar}}}{C_{\text{ar}}} + 0.0429 \frac{N_{\text{ar}}}{C_{\text{ar}}} \right), \quad (4)$$

where  $C_{\text{ar}}$ ,  $H_{\text{ar}}$ ,  $O_{\text{ar}}$ , and  $N_{\text{ar}}$  are the ratios of carbon, hydrogen, oxygen, and nitrogen, respectively, in the designed coal on an as-received basis (Table 2).

The total exergy loss  $I_{\text{total}}$  is the sum of the exergy losses  $I_j$  of component  $j$  (Liu et al., 2020c), and the equations for the components are listed in Table 3.

$$I_j = m_j i_j, I_{\text{total}} = \sum I_j \quad (5)$$

Our newly developed numerical model is not only suitable for sCO<sub>2</sub> coal-fired power plants but also for general cycle analysis. To verify the accuracy of the proposed model, cycle performances were compared based on computational outcomes of the Tang's model (Fan et al., 2020) and Dostal's model (Dostal, 2004). For comparison, an RC cycle was used; the control parameters, such as the main vapor parameters at the turbine and compressor inlets, and other assumptions were identical to those in Refs. (Dostal, 2004; Fan et al., 2020). Fig. 3 shows the  $T$ - $s$  curve, where  $s$  is the entropy, and comparison results. The deviations in thermal efficiencies using the three different models are less than 1%. The deviations were relatively large at lower turbine inlet pressure, such as 15 MPa, owing to uncertainties in the calculations of pressure drop in the components.

#### 3.2. Computation of sCO<sub>2</sub> boiler

Fig. 4a and b show the arrangements of the heaters in the total flow mode (TFM) and PFM, respectively. For the PFM, the flow rate and length of each module were reduced to half of those for the TFM. For example, Heater 1 consists of Part1 and SH1 in the TFM, whereas Heater 1 is decoupled into Part1, Part2, SH1, and SH2 in the PFM. For the computation of the sCO<sub>2</sub> boiler, two assumptions are made: no leakage of air or flue gas and uniform heat flux over the furnace width. Here, we provide a summary of the computations for the sCO<sub>2</sub> boiler; detailed

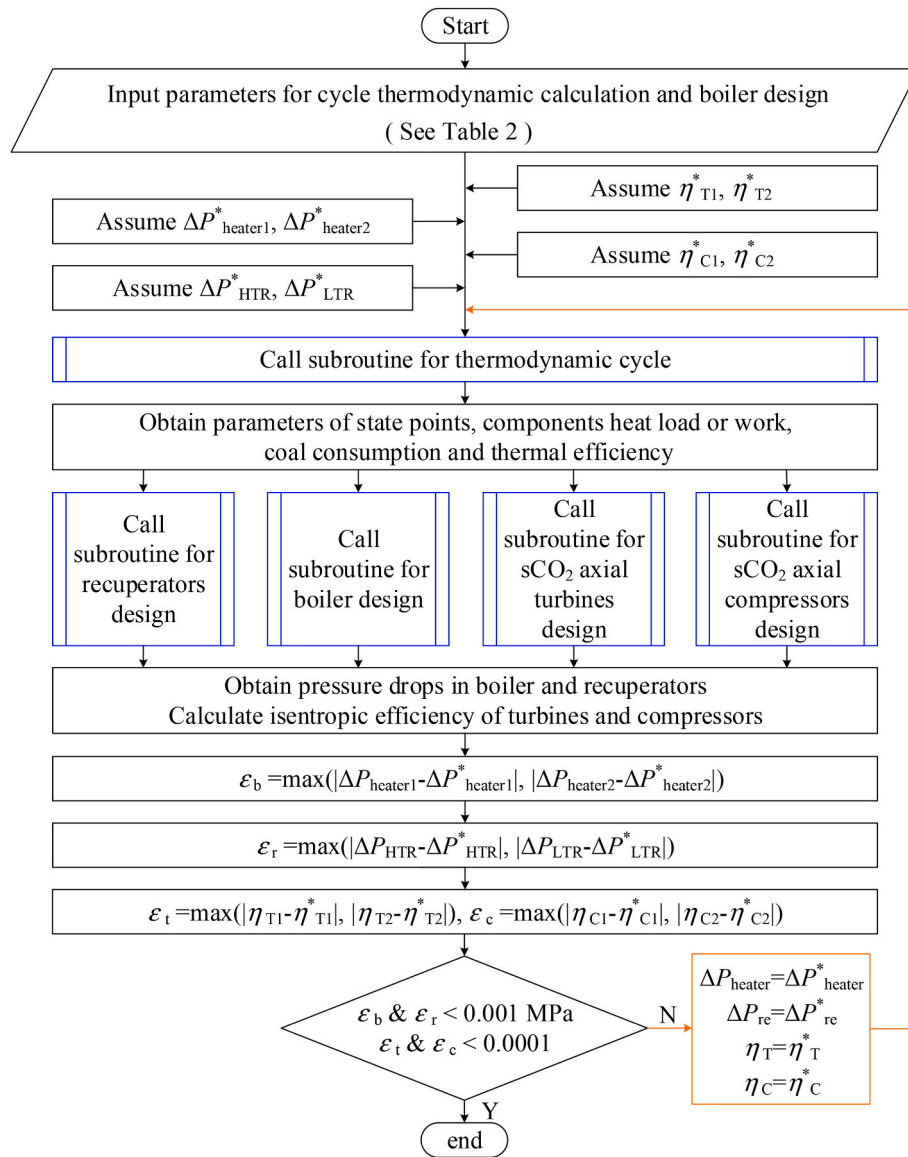


Fig. 2. Numerical calculations for cycle coupling with boiler, recuperators, turbines and compressors.

Table 1  
Parameters for the cycle computations.

parameters	values
boiler type	pulverized coal boiler
net power ( $W_{net}$ )	(100–1000) MWE
inlet temperature of compressor C1 ( $T_1$ )	32 °C
inlet pressure of compressor C1 ( $P_1$ )	7.6 MPa
inlet temperature of turbine T1 and T2 ( $T_5$ and $T_5'$ )	620 °C
inlet pressure of turbine T1 ( $P_1$ )	30 MPa
pinch temperature difference in LTR and MTR ( $\Delta T$ )	10 K
primary air temperature entering air preheater	31 °C
primary air temperature leaving air preheater	320 °C
ratio of primary air flow rate to the total air flow rate	19%
secondary air temperature entering air preheater	23 °C
ratio of secondary air flow rate to the total air flow rate	81%
environment temperature ( $T_0$ )	20 °C
excess air coefficient ( $\alpha$ )	1.2
pinch temperature difference between flue gas and CO <sub>2</sub> at point e ( $\Delta T_e$ )	40 K
pinch temperature difference between flue gas and CO <sub>2</sub> at point 4b ( $\Delta T_{4b}$ )	30 K

Table 2  
Properties of the designed coal (Xu et al., 2018; Wang et al., 2022).

$C_{ar}$	$H_{ar}$	$O_{ar}$	$N_{ar}$	$S_{ar}$	$A_{ar}$	$M_{ar}$	$V_{daf}$	$Q_{LHV}$
61.70	3.67	8.56	1.12	0.60	8.80	15.55	34.73	23442

C (carbon), H (hydrogen), O (oxygen), N (nitrogen), S (sulfur), A (ash), M (moisture), V (volatile).

Subscripts ar, d, af mean as received, dry and ash free,  $C_{ar} + H_{ar} + O_{ar} + N_{ar} + S_{ar} + A_{ar} + M_{ar} = 100$ .

information can be found in Ref. (Liu et al., 2020c).

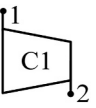
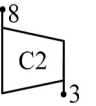
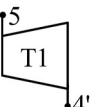
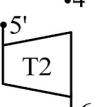
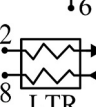
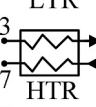
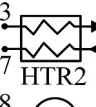

Based on Ref. (Fan, 2014), the flue gas temperature  $T'$  at the furnace outlet is

$$\theta' = \frac{T'}{T_{th}} = \frac{1}{1 + M(\epsilon^{syn}/Bo)^{0.6}}, \quad (6)$$

where  $\theta'$  is the dimensionless flue gas temperature at the furnace outlet,  $T_{th}$  is the adiabatic combustion temperature,  $Bo$  is the Boltzmann number  $5.67 \times 10^{-8} \text{ W}/(\text{m}^2\text{K}^4)$ , and  $\epsilon^{syn}$  is the furnace emissivity.

The thermal load of the furnace is given by

**Table 3**  
Equations for components in the cycle (Liu et al., 2020c).

components	equations and exergy destructions
	$\eta_{c,s} = \frac{h_{2s} - h_1}{h_2 - h_1}, w_{C1} = (1 - x_{C2})(h_2 - h_1); i_{C1} = w_{C1} - (1 - x_{C2})(e_2 - e_1)$
	$\eta_{c,s} = \frac{h_{3s} - h_8}{h_3 - h_8}, w_{C2} = x_{C2}(h_3 - h_8); i_{C2} = w_{C2} - x_{C2}(e_3 - e_8)$
	$\eta_{t,s} = \frac{h_5 - h_4}{h_5 - h_{4s}}, w_{T1} = h_5 - h_4; i_{T1} = e_5 - e_4 - w_{T1}$
	$P_5 = \sqrt{P_3 P_6}, \eta_{t,s} = \frac{h_5 - h_6}{h_5 - h_{6s}}, w_{T2} = h_5 - h_6; i_{T2} = e_5 - e_6 - w_{T2}$
	$T_8 = T_2 + \Delta T_{LTR}, x_{C2} = 1 - \frac{h_7 - h_8}{h_3 - h_2}, i_{LTR} = e_7 - e_8 - (1 - x_{C2})(e_3 - e_2)$
	$T_7 = T_3 + \Delta T_{HTR}, (1 - x_{EAP})(h_6 - h_7) = (1 - x_{Heater\ 4})(h_4 - h_3); i_{HTR} = (1 - x_{EAP})(e_6 - e_7) - (1 - x_{Heater\ 4})(e_4 - e_3)$
	$x_{EAP}(h_{6b} - h_7) = x_{Heater\ 4}(h_{4b} - h_3); i_{HTR2} = x_{EAP}(e_{6b} - e_7) - x_{Heater\ 4}(e_{4b} - e_3)$
	$i_{Cooler} = (1 - x_{C2})(e_8 - e_1)$

$$Q_R = \varphi(VC)_{av} T_{th} \left(1 - \frac{T^*}{T_{th}}\right), \quad (7)$$

where  $(VC)_{av}$  is the average specific heat of flue gas.

The average heat flux  $q_{ave}$  is as follows:

$$q_{ave} = \frac{Q_R}{S}, \quad (8)$$

where  $S$  is the heat transfer area of heaters below the furnace exit.

Pressure drop in the boiler tubes includes the friction component ( $\Delta P_f$ ), gravity component ( $\Delta P_g$ ), and acceleration component ( $\Delta P_a$ ).

$$\Delta P = \Delta P_f + \Delta P_g + \Delta P_a \quad (9)$$

$$\Delta P_f = \int_{z_{j-1}}^{z_j} \frac{f}{d_i} \frac{G^2}{2\rho} dz, \Delta P_g = \int_{z_{j-1}}^{z_j} \rho g dz, \Delta P_a = G^2 \left(\frac{1}{\rho_o} - \frac{1}{\rho_i}\right), \quad (10)$$

where  $G$  is the mass flux and  $\rho$  is the density. From Ref. (Wang et al., 2014), the friction coefficient  $f$  is

$$f = \frac{1}{3.24 \lg^2 \left[ \left(\frac{\Delta/d_i}{3.7}\right)^{1.1} + \frac{6.9}{Re} \right]}, \quad (11)$$

where  $\Delta$  is the absolute wall roughness.

sCO<sub>2</sub> boilers are currently in the research and development stages. However, experimental data are not available for large-scale sCO<sub>2</sub> boilers. A comparison was performed between the computation results for the sCO<sub>2</sub> boiler and the design standard for a commercial water-steam boiler (Fan, 2014). For both the sCO<sub>2</sub> and water-steam boilers, the heat flux of the heater surface depends strongly on the fire temperature of the furnace, but weakly on the temperature of the working fluids (Liu et al., 2022). Fig. 5a shows the calculated heat fluxes of heater surface,  $q_A$ , varying in the range of (4.0–4.1) MW/m<sup>2</sup> corresponding to the  $W_{net}$  range of (100–1000) MW/m<sup>2</sup> for sCO<sub>2</sub> boiler. This variation range of  $q_A$  for sCO<sub>2</sub> boiler is consistent with the range of (3.8–4.5) MW/m<sup>2</sup> for water-steam boiler. At the three power capacities of 100 MWe, 300 MWe, and 600 MWe, the calculated volume heat flux  $q_V$  values are 124.1 kW/m<sup>3</sup>, 99.5 kW/m<sup>3</sup>, and 83.2 kW/m<sup>3</sup>, respectively. These  $q_V$  values for the sCO<sub>2</sub> boiler are on the bottom margin of  $q_V$  for water-steam boilers (Fig. 5b).

### 3.3. Computation of recuperators

#### 3.3.1. Fluid network of PCHE-based recuperators

PCHE-based recuperators have attracted widespread attention in sCO<sub>2</sub> power generation because of their compactness (Dyreby et al., 2014). Owing to the shipping requirements (Jiang et al., 2018a), the thermal load of a single recuperator is limited. Therefore, thermal integration of various PCHE units is necessary for large-scale heat recovery. Fig. 6 shows the fluid network for such an integration, where the red and blue lines represent the hot and cold sides of the CO<sub>2</sub> fluid, respectively. Pipes with larger and smaller diameters represent the main and branch pipes, respectively. Considering the hot side as an example, the CO<sub>2</sub> steam with a total flow rate  $M_{h,in}$  and temperature  $T_{h,in}$  at the inlet of the main pipe flows into the main pipe and dissipates its flow rate to the  $N$  PCHE units in sequence, noting different flow rates  $m_i$  in different PCHE units. After the hot-side CO<sub>2</sub> transfers its heat to the cold-side CO<sub>2</sub>, the CO<sub>2</sub> steam is collected in the main pipe and finally leaves the main pipe with parameters  $M_{h,out}$  and  $T_{h,out}$ . The following assumptions have been made: (i) no CO<sub>2</sub> leakage occurs across the hot and cold sides, (ii) no heat loss occurs in pipelines, (iii) the total flow rate

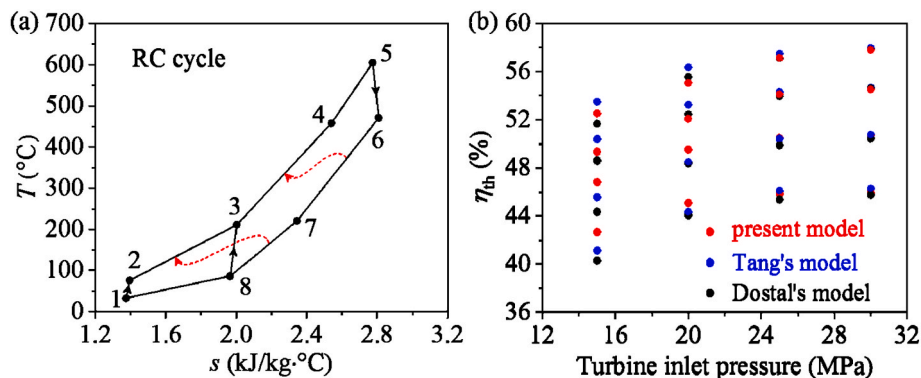


**Fig. 3.** Comparison of thermal efficiencies for the RC cycle based on the present model, the Tang's model (Fan et al., 2020) and the Dostal's model (Dostal, 2004) (a: T-s curve; b: thermal efficiencies versus turbine inlet pressures).

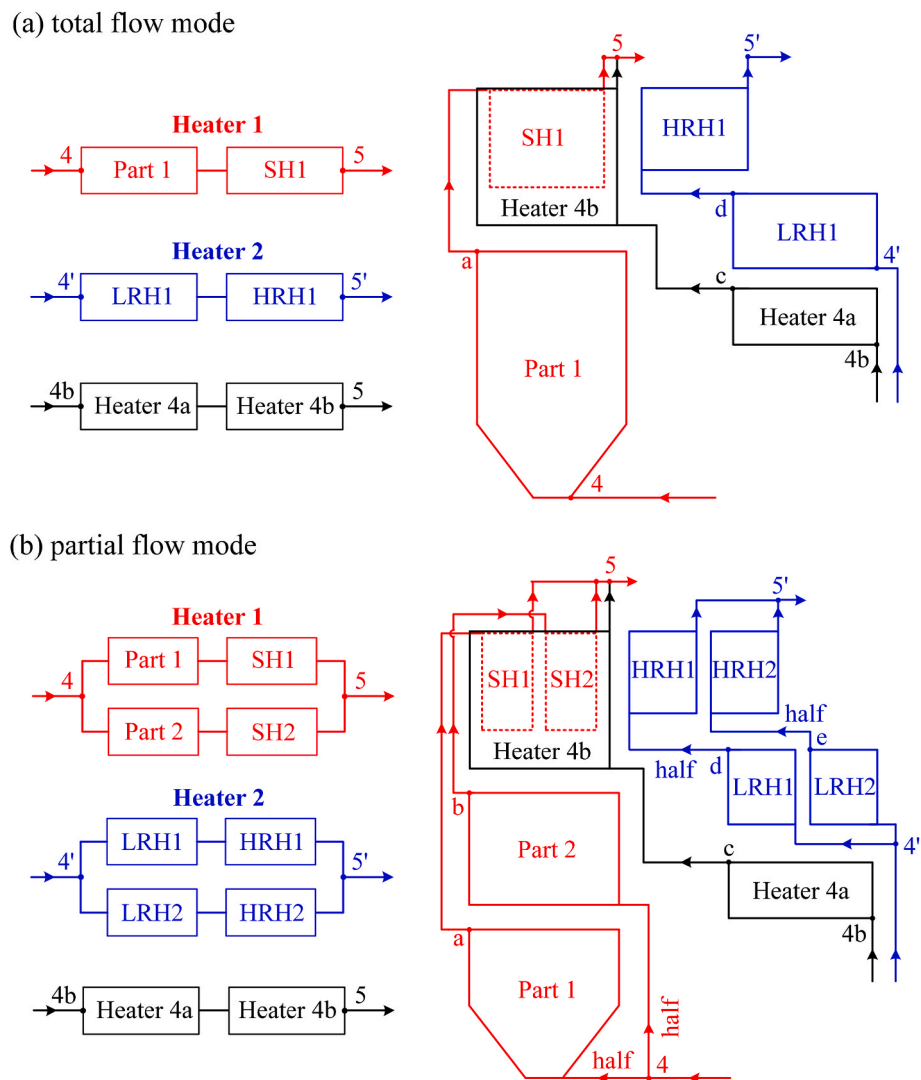


Fig. 4. The total flow mode (TFM) and partial flow mode (PFM) adapted to the boiler design (This figure is cited from Ref. (Liu et al., 2020c). Copyright 2020, Elsevier).

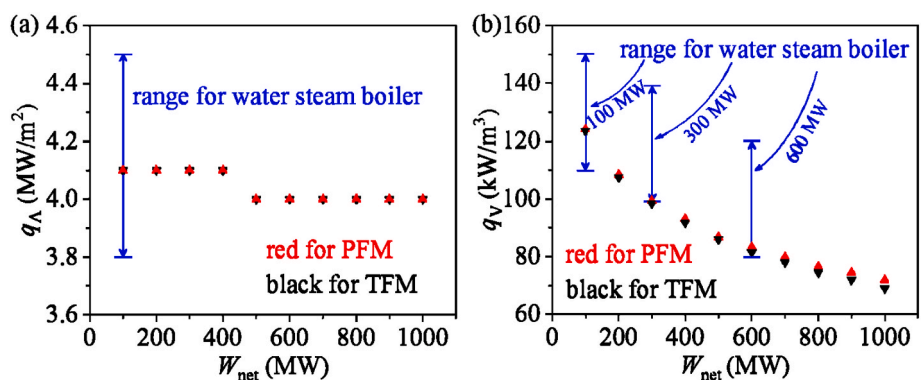


Fig. 5. Comparison of thermal loads between sCO<sub>2</sub> boiler and water-steam boiler (a: surface heat fluxes  $q_A$ , the reference value is (3.8–4.5) MW/m<sup>2</sup> for water-steam boiler; b: Volume heat flux  $q_V$ , a reference value is (110–150) kW/m<sup>3</sup> for water-steam boiler at  $W_{net} = 100$  MWe, (100–140) kW/m<sup>3</sup> at  $W_{net} = 300$  MWe and (80–120) kW/m<sup>3</sup> at  $W_{net} = 600$  MWe).

is re-distributed in the  $N$  PCHE units based on the pressure balance in the fluid network, and (iv) the frictional pressure drop in the pipeline is no more than 0.6 kPa/m (Heatric, 2017).

As the arrangements of the hot and cold sides are similar, the

equations are provided for the hot side only (Fig. 6). The equations for mass conservation are as follows:

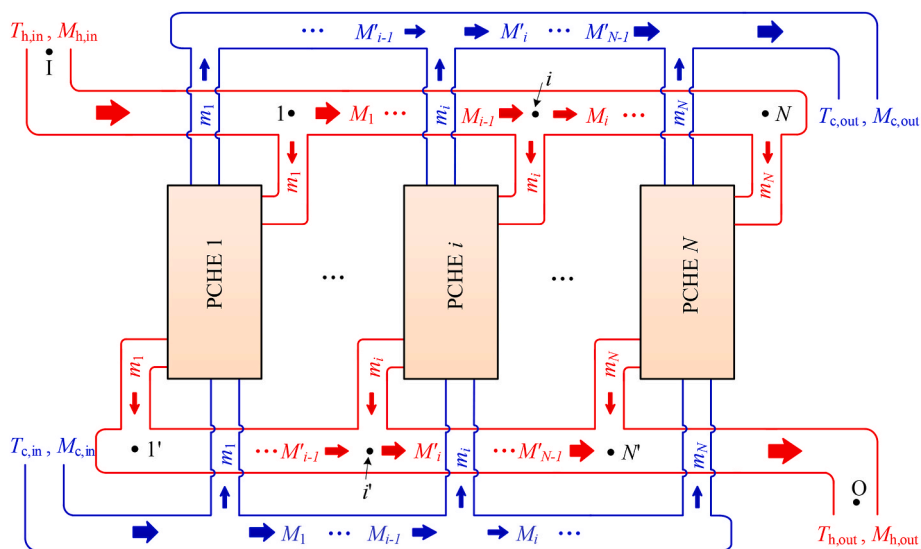


Fig. 6. Thermal integration of recuperators heat exchangers.

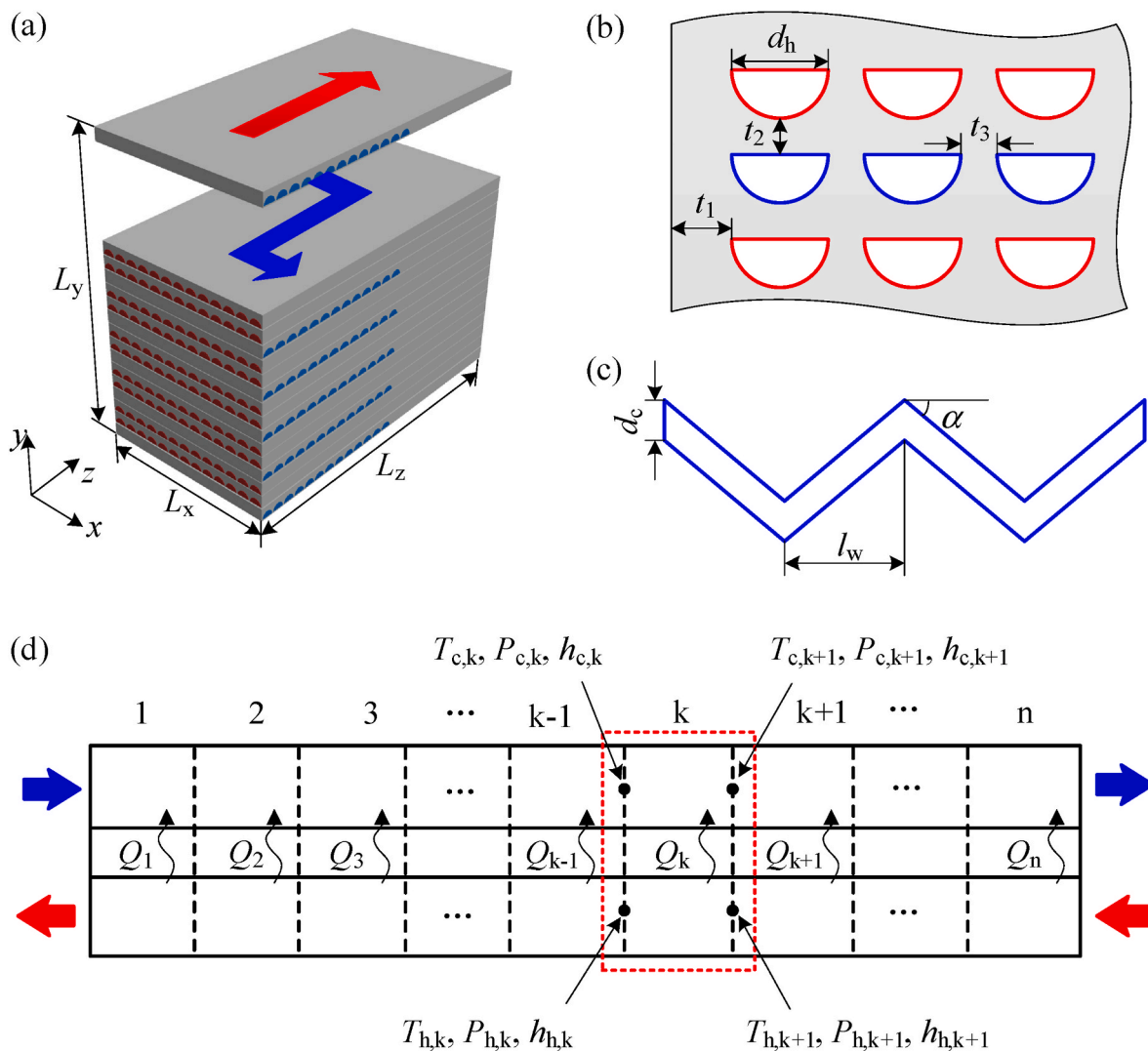


Fig. 7. The PCHE model based on Refs. (Liu, 2022; Jiang et al., 2018b). (a) 3D model for the PCHE, (b) geometry size over the cross section, (c) geometry size of a zigzag channel, (d) discretized microtube in the PCHE model.

$$\begin{cases} M_{i-1} = M_i + m_i, i = 2, 3, \dots, N-1 \\ M_{h,in} = M_{i-1} + M'_{i-1}, i = 1, 2, \dots, N-1 \\ M_{h,in} = M_1 + m_1 \\ M_{N-1} = m_N \\ M_{h,in} = M_{h,out} \end{cases}, \quad (12)$$

where the subscript  $i$  represents the  $i$ th PCHE unit.

Because I and O are common pressure points, each branch connecting the two points shares the same pressure drop, as represented by

$$\Delta P_{IO} = \Delta P_{IiO}, i = 1, 2, \dots, N, \quad (13)$$

where  $\Delta P_{IO}$  is the total pressure drop containing the frictional components in the pipeline and PCHE channels, as well as the local pressure drop when the fluid flows across different elements. The equations for these calculations are based on Refs. (Saber et al., 2009; Liu, 2022). Owing to the varied physical properties of CO<sub>2</sub>, a discretization method was applied.

### 3.3.2. Optimal design of PCHEs

The hot and cold plates were separated by etched channels and assembled via diffusion bonding (Fig. 7a). The cold and hot sCO<sub>2</sub> fluids flow counter-currently. A PCHE unit has a characteristic size of  $L_x \times L_y \times L_z$ , wherein  $L_x$  and  $L_y$  should be smaller than 0.6 m and 8 m, respectively (Linares et al., 2018).  $R_p$  is the ratio of the number of hot plates to that of cold plates ( $R_p = 2$ , in this study). The PCHE channels have semi-circular cross sections characterized by a diameter of  $d_h$  (Fig. 7b). Edge width  $t_1$ , wall thickness  $t_2$ , and ridge width  $t_3$  were determined based on the allowed stress and corrosion of the material. Fig. 7c shows the zigzag channels with  $d_c = d_h$ , where  $d_c$  is the characteristic diameter of the cold channels. The wave angle  $\alpha$  is in the range of 25–40° (Jiang et al., 2018b), with  $\alpha = 32.5^\circ$  in this study, and the channel width was 4.5 mm. The primary parameters are listed in Table 4. The thermal load between two neighboring discretization points (Jiang et al., 2018b) is given by

$$Q_k = m_h(h_{h,k+1} - h_{h,k}) = m_c(h_{c,k} - h_{c,k+1}) \quad (14)$$

$Q_k$  can also be expressed as follows:

$$Q_k = \text{LMTD}_k U_k A_k, \quad (15)$$

where LMTD is the logarithmic mean temperature difference,  $U$  and  $A$  are the heat transfer coefficient and heat transfer area, respectively, which are calculated as follows (Kim et al., 2016):

$$\text{LMTD}_k = \frac{(T_{h,k} - T_{c,k}) - (T_{h,k+1} - T_{c,k+1})}{\ln[(T_{h,k} - T_{c,k}) / (T_{h,k+1} - T_{c,k+1})]} \quad (16)$$

$$U_k = \frac{1}{h_{c,k}} + \frac{t_c}{k_{w,k}} + \frac{1}{h_{h,k} R_p} \quad (17)$$

$$t_c(d_c + t_3) = (d_c + t_3) \times \left( \frac{d_c}{2} + t_2 \right) - \frac{\pi d_c^2}{8} \quad (18)$$

**Table 4**  
Geometry parameters for PCHEs (Jiang et al., 2018b).

parameters	values
channel type	zigzag
diameter ( $d_c$ and $d_h$ )	2.0 mm
angle ( $\alpha$ )	32.5°
length of the channel ( $l_w$ )	4.5 mm
ratio of the number of hot plates to that of cold plates	2
width of a PCHE module ( $L_x$ )	0.6 m
upper limit of the height for a PCHE unit ( $L_{y,ml}$ )	8.0 m

$$A_k = \frac{1}{1 + R_p} N_c N_p \left( 1 + \frac{\pi}{2} \right) d_c L_{c,k}, \quad (19)$$

where  $t_e$  is the equivalent wall thickness;  $h_{c,k}$  and  $h_{h,k}$  are the heat transfer coefficients on the hot and cold sides of the discretization unit  $k$ , respectively;  $k_{w,k}$  is the thermal conductivity of the metal wall;  $N_p$  is the number of plates;  $N_c$  is the number of channels for each cold plate; and  $L_{c,k}$  is the segment length of the channels.

Kim et al. (2016) proposed the correlations of Nusselt number and friction factor with Reynolds number  $Re$  in the range of 2000–58000.

$$Nu = (0.0292 \pm 0.0015) Re^{0.8138 \pm 0.0050} \quad (20)$$

$$f = (0.2515 \pm 0.0097) Re^{-0.2031 \pm 0.0041} \quad (21)$$

The PCHE of the DOE-sponsored STEP program was modeled to validate the proposed PCHE model. A comparison of the simulation results with those reported in literature (Jiang et al., 2018b) is presented in Table 5. The input parameters included the thermal load  $Q$  of the PCHE, inlet temperature  $T_{c,i}$  and pressure  $P_{c,i}$  of the cold sides, outlet temperature  $T_{h,o}$  and pressure  $P_{h,o}$  of the hot side, and width  $L_x$  and height  $L_y$  of the PCHE unit. The relative deviation of the length  $L_z$  was 2.32%, and the relative errors of other parameters were less than 1%. The calculated values were in good agreement with the STEP design values.

### 3.4. sCO<sub>2</sub> axial turbines

Radial and axial turbines are suitable for small-scale and large-scale power generation, respectively (Fleming et al., 2012). Axial turbines were used in this study; the physical model is shown in Fig. 8a. The more stages the turbine has, the higher the turbine efficiency and fabrication cost (Wang et al., 2023). Based on this tradeoff, three stages were applied. In Fig. 8a, S represents the stationary blade, which increases the tangential velocity of the gas in the rotating direction; R represents the rotating blade, which converts the kinetic energy of the gas into torque;  $D$  is the hub radius;  $r$  is the radius of the blade tip;  $b$  is the blade height; and  $a$  is the axial chord length. Fig. 8b shows the  $h$ - $s$  diagram and Fig. 8c shows the velocity triangle for the first stage expansion, where nodes 1 and 2 represent the stator inlet and outlet, respectively. Node 3 represents the rotor outlet, and  $\alpha$  and  $\beta$  represent the absolute and relative flow angles, respectively.

The isentropic expansion is indicated by the dashed line from Node 1 to Node 3ss, but the practical expansion is an entropy-rise process, indicated by the line from Node 1 to Node 3. The isentropic efficiency is given by

$$\eta_{T,1} = \frac{h_1 - h_3}{h_1 - h_{3ss}} \quad (22)$$

The total-to-total efficiency of a three-stage axial flow turbine is as follows (Wang et al., 2023):

**Table 5**  
Comparison between the present PCHE model and STEP's model (Jiang et al., 2018b).

	STEP (10 MWe)	Present model	Relative error (%)
$T_{h,i}/^\circ\text{C}$	578.15	578.21	0.01%
$T_{c,o}/^\circ\text{C}$	532.10	532.20	0.04%
$P_{h,i}/\text{MPa}$	8.96	8.97	0.11%
$\Delta P_h/\text{MPa}$	1.08	1.07	0.93%
$\Delta P_c/\text{MPa}$	1.40	1.39	0.71%
$N_p$	4231	4230	0.02%
$N_c$	109	110	0.92%
$L_z/\text{m}$	0.86	0.88	2.32%

Note: the input parameters are  $Q = 45.15$  MW,  $P_{h,o} = 8.96$  MPa,  $P_{c,i} = 23.75$  MPa,  $P_{c,o} = 23.61$  MPa,  $T_{h,o} = 192.00$  °C,  $T_{c,i} = 181.95$  °C,  $L_x = 0.35$  m,  $L_y = 6.88$  m.



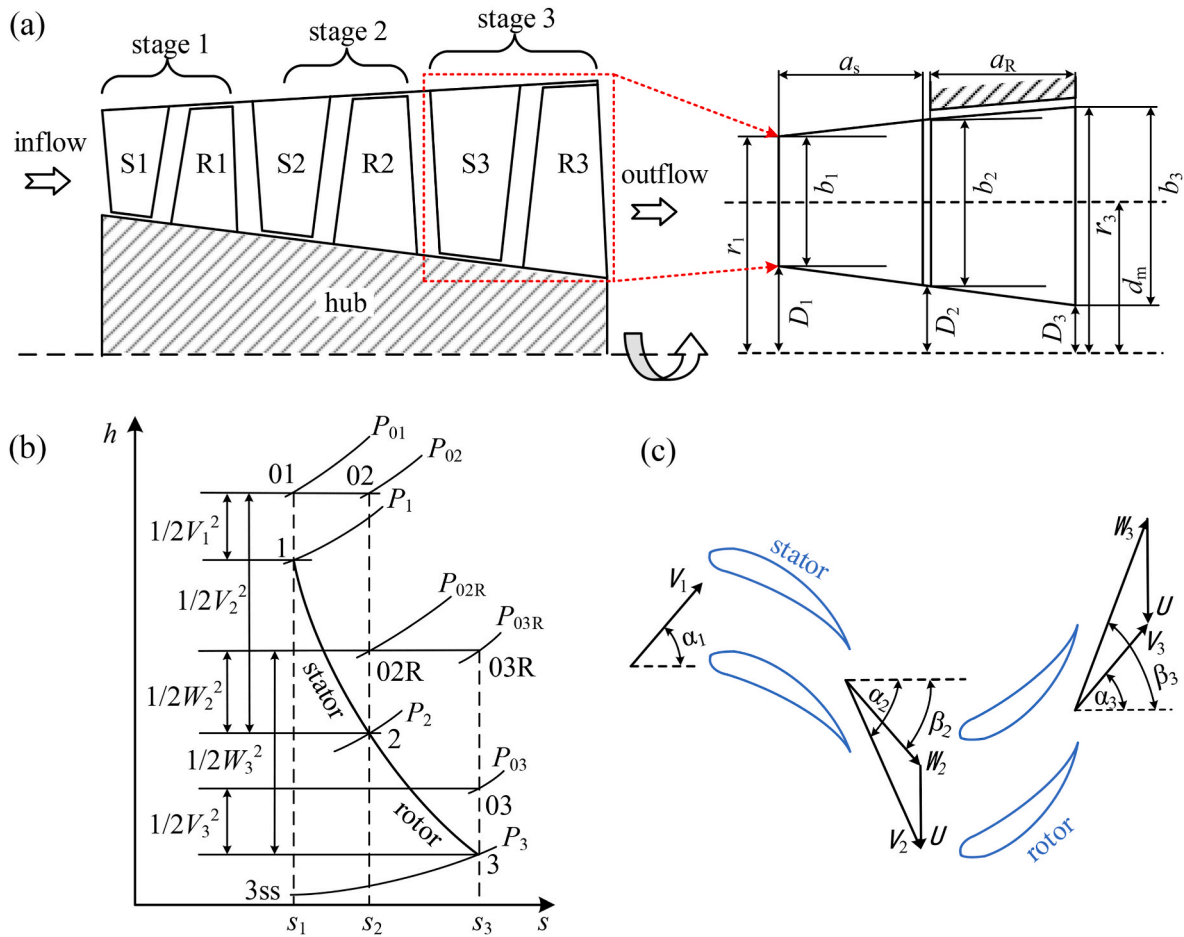


**Fig. 8.** Working principle of sCO<sub>2</sub> axial flow turbine. (a) multi-stages axial flow turbine, (b) the *h-s* curve in the first stage of turbine (Aungier, 2005), (c) velocity triangles due to expansion (Aungier, 2005).

$$\eta_u = \frac{h_1 - h_7}{h_1 - h_{7ss}}, \quad (23)$$

where  $h_{7ss}$  is the maximum enthalpy at the turbine outlet according to isentropic expansion.

$P_{02}$  at Node 2 is given by

$$P_{02} = f\left(h_2 + \frac{V_2^2}{2}, s_2\right), \quad (24)$$

where  $h_2 + \frac{V_2^2}{2}$  is the total enthalpy, and  $V_2$  is the absolute velocity.

Alternatively, replacing  $V_2$  by the relative velocity  $W_2$  (Fig. 8c) yields the following:

$$P_{02R} = f\left(h_2 + \frac{W_2^2}{2}, s_2\right) \quad (25)$$

A similar method was applied to nodes 1 and 3; however,  $P_{01R}$  could not be defined because no relative velocity existed at this node. The mean-line method was used for one-dimensional turbine calculations. The necessary assumptions are: (i)  $\varphi$ ,  $\psi$ , and  $R$  are the same for different stages, (ii) the enthalpy drop is the same for different stages, (iii) the circumferential velocity  $U$  and radial velocity  $V_x$  are the same for different stages, and (iv) the flow angle is the same for different stages.

The  $\varphi$ ,  $\psi$ , and  $R$  allow for the calculation of absolute and relative flow angles, playing critical roles in the turbine simulation. The values set for these three parameters are listed in Table 6;  $\varphi$  and  $\psi$  are recommended to be 0.4 and 0.9, respectively, and  $R$  is recommended to be within the range of 0.45–0.50 (Da et al., 2014). In this study,  $R = 0.49$  is used.

**Table 6**  
Parameters for the turbines design.

Parameters	Values
flow coefficient $\varphi$ (Da et al., 2014)	0.4
load coefficient $\psi$ (Da et al., 2014)	0.9
the degree of reaction $R$	0.49
the number of stages	3

$$\begin{cases} \alpha_2 = \arctan\left(\frac{1 - R + \psi/2}{\varphi}\right), \alpha_3 = \arctan\left(\frac{1 - R - \psi/2}{\varphi}\right) \\ \beta_2 = \arctan\left(\frac{-R - \psi/2}{\varphi}\right), \beta_3 = \arctan\left(\frac{-R + \psi/2}{\varphi}\right) \end{cases} \quad (26)$$

The rotating speed of the turbine  $n$  is calculated as follows (Aungier, 2005):

$$N_s = \frac{n\sqrt{Q}}{(h_1 - h_{7ss})^{3/4}}, \quad (27)$$

where  $N_s$  is the specific speed, and  $Q$  is the volume flow rate;  $n$  is influenced by the power capacity. In China, the alternating current frequency is 50 Hz, which corresponds to a speed of 3000 rpm. To satisfy this requirement, gearboxes are necessary when the turbine speed exceeds 3000 rpm. It is inconvenient to use a gearbox when the power generation is greater than 450 MWe for a single turbine (Bidkar et al., 2016). Thus,  $n = 3000$  rpm was applied for turbines with powers greater than 450 MWe, and  $n$  was determined for powers less than 450 MWe.

The peripheral velocity  $U$  and meridional velocity  $V_x$  are determined as follows:

$$h_3 = h_1 - \frac{(h_1 - h_7)}{3} \tag{28}$$

$$U = \sqrt{(h_1 - h_3)/\psi}, V_x = U\varphi \tag{29}$$

$$\begin{cases} V_2 = V_x/\cos \alpha_2, V_3 = V_x/\cos \alpha_3, V_1 = V_3 \\ W_2 = V_x/\cos \beta_2, W_3 = V_x/\cos \beta_3 \end{cases} \tag{30}$$

Based on the calculated geometric parameters, an appropriate loss model was selected, and the isentropic efficiency of the turbine was determined through the iteration process. In this study, the Aungier model (Ainley and Mathieson, 1951) was selected owing to its foundation in the AM (Ainley and Mathieson, 1951) and AMDC (Dunham and Came, 1970) models and its reference to the KO model (Kacker and Okapuu, 1982). The calculation of losses can be found in a previous study (Da et al., 2014).

A validation of the turbine model is presented; here, the simulation results were compared with those for high-pressure and low-pressure turbines reported by the TPRI (Li et al., 2019b), which are listed in Table 7. They designed a 5 MWe sCO<sub>2</sub> pilot test loop driven by a natural gas boiler (Li et al., 2019b). Two stages were involved in the two turbines with a rotating speed of 9000 rpm. The degrees of reaction of the high-pressure and low-pressure turbines were 0.45 and 0.2, respectively. Other input parameters included the inlet temperature and pressure, pressure ratio, and mass flow rate. The maximum relative error was 5.76%, which is acceptable.

### 3.5. sCO<sub>2</sub> axial compressors

The sCO<sub>2</sub> compressor pumped sCO<sub>2</sub> fluid in the cycle. It is necessary to estimate the dimensions and velocity triangle at each stage by simultaneously solving the conservation equations for mass, momentum, and energy under the given inlet conditions (Aungier, 2003). Here, the axial-flow compressors were considered. Fig. 9a shows the physical model, where R represents the rotating blade, which converts the kinetic energy of the blade into the energy of sCO<sub>2</sub>, and S represents the stationary blade, which converts the kinetic energy of sCO<sub>2</sub> into its static pressure. The number of stages for the compressor  $n$  is typically larger than that for the turbine. Eight and five stages were applied to C1 and C2, respectively. The definitions of the geometric parameters of the compressor can be referenced to those of the turbine. Fig. 9b and c show the  $h$ - $s$  diagram and velocity triangle, respectively, for the first stage.

Isentropic compression is indicated by the dashed line from Node 1 to Node 3ss. In practice, entropy increases during compression, as indicated by the line from Node 1 to Node 3. The isentropic efficiency is given by

$$\eta_{C,1} = \frac{h_1 - h_3}{h_1 - h_{3ss}} \tag{31}$$

The design methodology for the compressor is similar to that for the turbine. This method focused on one-dimensional calculation. The definitions and assumptions for the parameters, including the enthalpy drop, circumferential velocity  $U$ , radial velocity  $V_x$ , flow angles, flow coefficient  $\varphi$ , work coefficient  $\psi$ , and degree of reaction  $R$ , were identical for different stages. Notably,  $\varphi$ ,  $\psi$ , and  $R$  are important parameters for the design of the axial-flow compressor. To select suitable values for these parameters, not only the efficiency improvement but also the prevent stalling should be considered. The criterion developed by de Haller (Wang et al., 2004) can predict whether stalling occurs and is expressed as follows:

$$\sqrt{\frac{\varphi^2 + (\frac{\psi}{2} - R)^2}{\varphi^2 + (\frac{\psi}{2} + R)^2}} < 0.72 \tag{32}$$

Based on the optimum results, the recommended values for the three parameters were  $\varphi = 0.33$ ,  $\psi = 0.25$ , and  $R = 0.5$  (Table 8). The flow angle and rotating speed were calculated using Eqs. (26) and (27), respectively; peripheral velocity  $U$  and meridional velocity  $V_x$  were determined using Eqs. 28–30. Various loss models have been proposed (Aungier, 2003); therefore, care should be taken while selecting suitable loss models. Because the experimental data conformed to the Aungier model (Aungier, 2003), it was adopted in this study. The design outcomes predicted by the compressor model used in this study were compared with those reported in Ref. (Li et al., 2019a). A four-stage compressor with an inlet pressure of 7.6 MPa and pressure ratio of 4.33 was employed. The mass flow rate and rotating speed were 1392.0 kg/s and 3000 rpm, respectively. The comparison included several important geometric parameters. The deviations between the present predictions and the values reported in Ref. (Li et al., 2019a) were small, with a maximum deviation of 3.61% for the hub radius of the first stage rotor blade (Table 9).

## 4. Results and discussion

### 4.1. Effect of power capacities on thermal efficiencies of the system

The present study considered the sCO<sub>2</sub> cycle coupled with sCO<sub>2</sub> boilers, recuperator heat exchanger turbines, and compressors with  $W_{net}$  in the range of (100–1000) MWe. Fig. 10a shows the parabolic distribution of the thermal efficiency  $\eta_{th}$  versus the power capacity  $W_{net}$ . With increasing  $W_{net}$ ,  $\eta_{th}$  increases, reaches a maximum, and subsequently decreases. This variation trend is evidently different from the monotonous decrease in  $\eta_{th}$  over the entire  $W_{net}$  range for the cycle coupled with the sCO<sub>2</sub> boiler only (Fig. 10b). In other words, the cycle coupling with recuperators and turbomachinery changes the variation trend of the

**Table 7**  
Comparison between the present turbine model and TPRI's model (Li et al., 2019b).

parameters	T1			T2		
	TPRI	Present model	Relative error (%)	TPRI	Present model	Relative error (%)
inlet temperature (°C)	600	600	/	600	600	/
inlet pressure (MPa)	20.0	20.0	/	14.6	14.6	/
pressure ratio	1.32	1.32	/	1.71	1.71	/
mass flow rate (kg/s)	80.6	80.6	/	82.1	82.1	/
rotating speed (r/min)	9000	9000	/	9000	9000	/
number of stages	2	2	/	2	2	/
degree of reaction	0.45	0.45	/	0.2	0.2	/
first stage stator blade height (mm)	14.56	15.40	5.76	17.38	17.89	2.93
number of first stage stator blades	67	69	2.99	66	68	3.03
last stage stator blade height (mm)	17.27	17.40	0.75	23.65	22.86	4.37
number of last stage stator blades	67	68	1.49	65	66	1.54
isentropic efficiency (%)	77.07	76.47	0.78	79.21	78.87	0.43

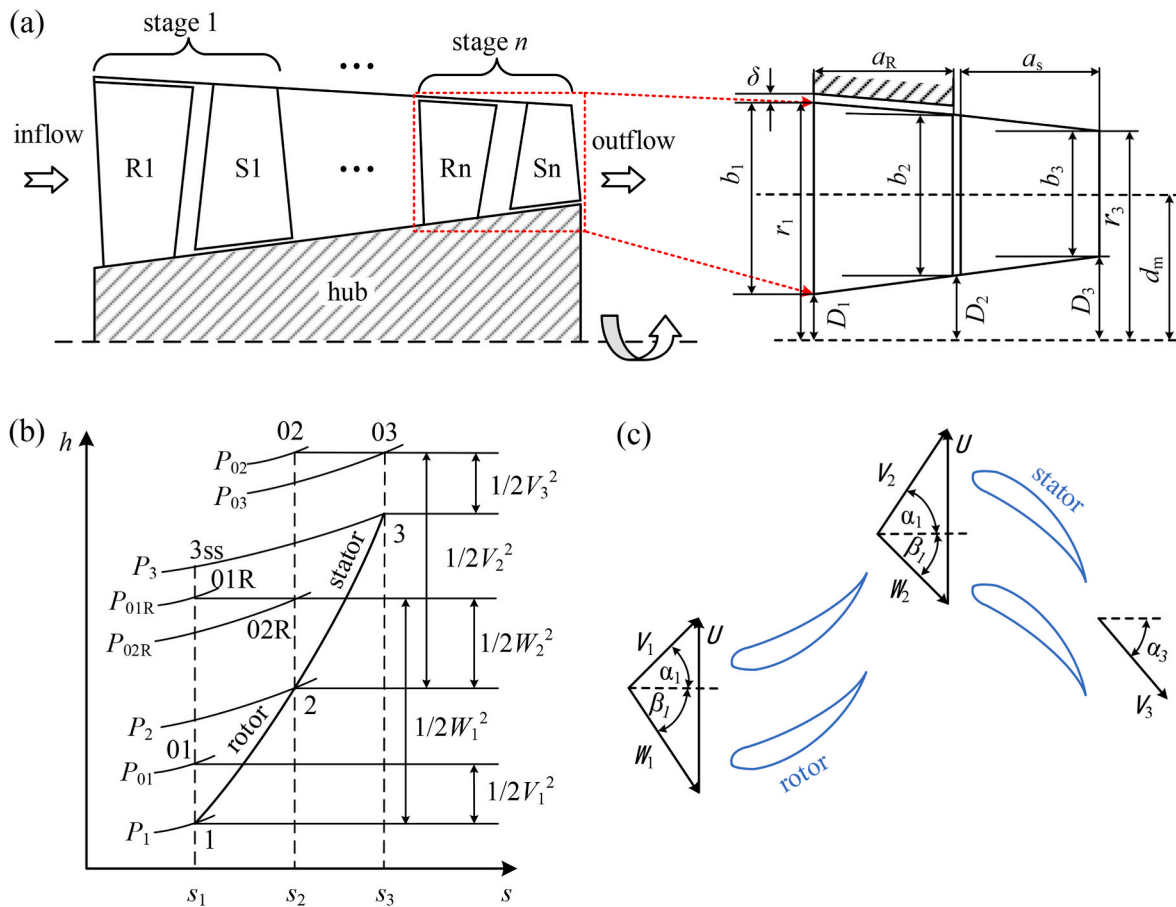


Fig. 9. Working principle of sCO<sub>2</sub> axial flow compressor. (a) multi-stages axial flow compressor, (b) the *h-s* curve in the first stage of compressor (Aungier, 2003), (c) velocity triangles due to compression (Aungier, 2003).

**Table 8**  
Parameters for the compressor design.

Parameters	Values
Flow coefficient $\varphi$	0.33
Load coefficient $\psi$	0.25
The degree of reaction <i>R</i>	0.5
the number of stages for C1	8
the number of stages for C2	5

efficiency curves. Practical sCO<sub>2</sub> power plants are likely to exhibit the performance curve shown in Fig. 10a. The maximum  $\eta_{th}$  occurs at  $W_{net}$  of 200 MWe when using the TFM, but occurs at  $W_{net}$  of 300 MWe when using the PFM.

Fig. 10a and b demonstrate the significant contribution of the PFM in improving the system performance. The difference in thermal efficiencies between the PFM and TFM increased with an increase in  $W_{net}$ . For example, this difference is 0.30% at  $W_{net} = 100$  MWe, but becomes 6.44% at  $W_{net} = 1000$  MWe (Fig. 10a), indicating that it is necessary to apply PFM for practical design of sCO<sub>2</sub> power plants. The PFM yielded insensitive variations in thermal efficiencies at various power capacities. The difference in efficiency was approximately 0.19% between  $W_{net}$  of 100 MWe and 1000 MWe (Fig. 10a). For the cycle coupled with the sCO<sub>2</sub> boiler only, the difference in efficiency was 1.80% between  $W_{net}$  of 100 MWe and 1000 MWe (Fig. 10b).

In Fig. 10a, the comprehensive effect was decoupled to consider the independent effect of each parameter on the thermal efficiency. Four curves are presented in Fig. 11, where the red curve represents the overall  $\eta_{th}$  curve, and the other three curves represent the effects of

**Table 9**  
Comparison between the present compressor model and TPRI's model (Li et al., 2019a).

parameters	TPRI	Present model	Relative error (%)
inlet temperature (°C)	32	32	/
inlet pressure (MPa)	7.6	7.6	/
pressure ratio	4.33	4.33	/
mass flow rate (kg/s)	1392.0	1392.0	/
rotating speed (r/min)	3000	3000	/
number of stages	4	4	/
first stage rotor exit width (mm)	140	138	1.42
hub radius of first stage rotor blade (mm)	166	160	3.61
tip radius of first stage rotor blade (mm)	340	335	0.15
last stage rotor blade width (mm)	178	176	1.18
hub radius of last stage rotor blade (mm)	145	141	2.76
tip radius of last stage rotor blade (mm)	480	474	1.25
isentropic efficiency (%)	85	83.9	1.29

pressure drop in the sCO<sub>2</sub> boiler, pressure drops in the sCO<sub>2</sub> boiler and recuperators, and turbine and compressor efficiencies. For both TFM and PFM, the varied turbine and compressor performances increased the thermal efficiency of the system with an increase in  $W_{net}$ . In contrast, the pressure drops in the sCO<sub>2</sub> boiler significantly decreased the thermal efficiency of the system with an increase in  $W_{net}$ . The efficiency curve considering the pressure drops in the sCO<sub>2</sub> boiler and recuperators exhibited a distribution similar to that considering the pressure drops in

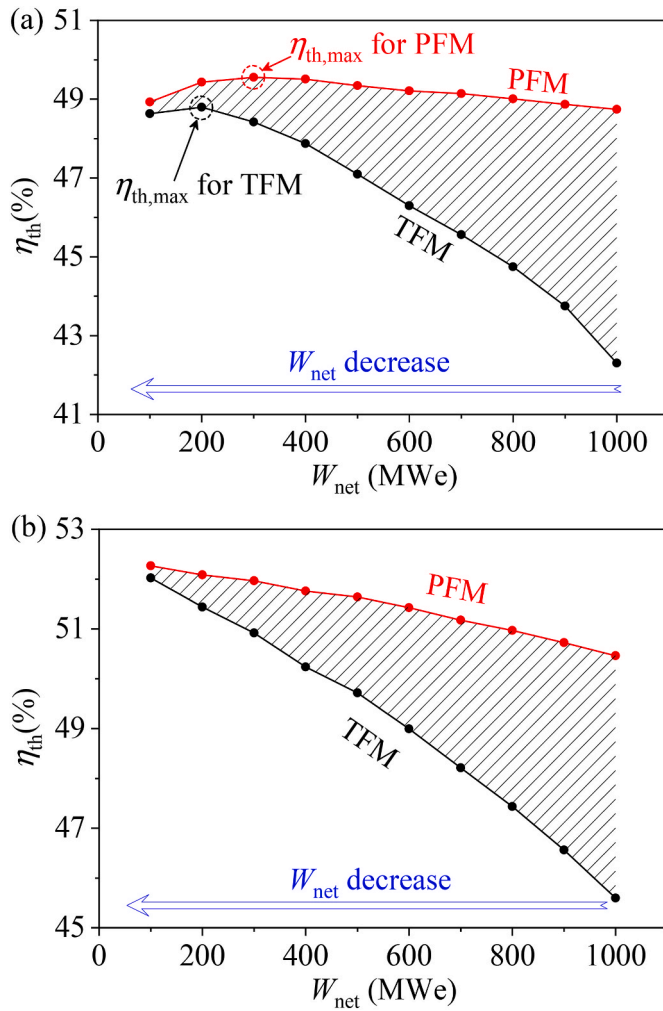


Fig. 10. Thermal efficiencies at different power capacities. (a) result of this paper, (b) result cited from Ref. (Liu et al., 2020c).

the sCO<sub>2</sub> boiler only, with further reduced thermal efficiencies. In summary, the parabolic distribution of the overall efficiency curve indicates a tradeoff between the improved performance of the turbines and compressors and the deteriorated performance of the sCO<sub>2</sub> boilers and recuperators at higher power capacities.

#### 4.2. Effect of power capacities on pressure drops

The compressor supplied the pressure head to maintain sCO<sub>2</sub> circulation in the system. Here, we analyzed the influence of the power capacities on the pressure drops.

##### 4.2.1. Pressure drop in sCO<sub>2</sub> boiler

The sCO<sub>2</sub> boiler consists of Heater 1, Heater 2, and Heater 4a (Fig. 4). Two modules are included in each heater for TFM, but more modules are included for PFM. Pressure drops are shown in Fig. 12, where  $\Delta P_{\text{boiler}} = \Delta P_{\text{Heater 1}} + \Delta P_{\text{Heater 2}}$ . For both modes, TFM and PFM, pressure drops increase with increase in power capacities owing to increased flow rates in the tubes of various heaters. It is observed that the  $\Delta P_{\text{Heater 1}}$  curve approaches the  $\Delta P_{\text{boiler}}$  curve, demonstrating the dominant contribution of  $\Delta P_{\text{Heater 1}}$ . Comparing Fig. 12a and b, pressure drops when using PFM are one magnitude smaller than those when using TFM. For example,  $\Delta P_{\text{boiler}}$  equals to 2.0 MPa at  $W_{\text{net}} = 1000$  MWe for PFM, but equals to 10.5 MPa at the same power capacity for TFM, which is not acceptable for practical engineering.

As shown in Fig. 1,  $P_2$  and  $P_5$  are the pressures at the compressor C1

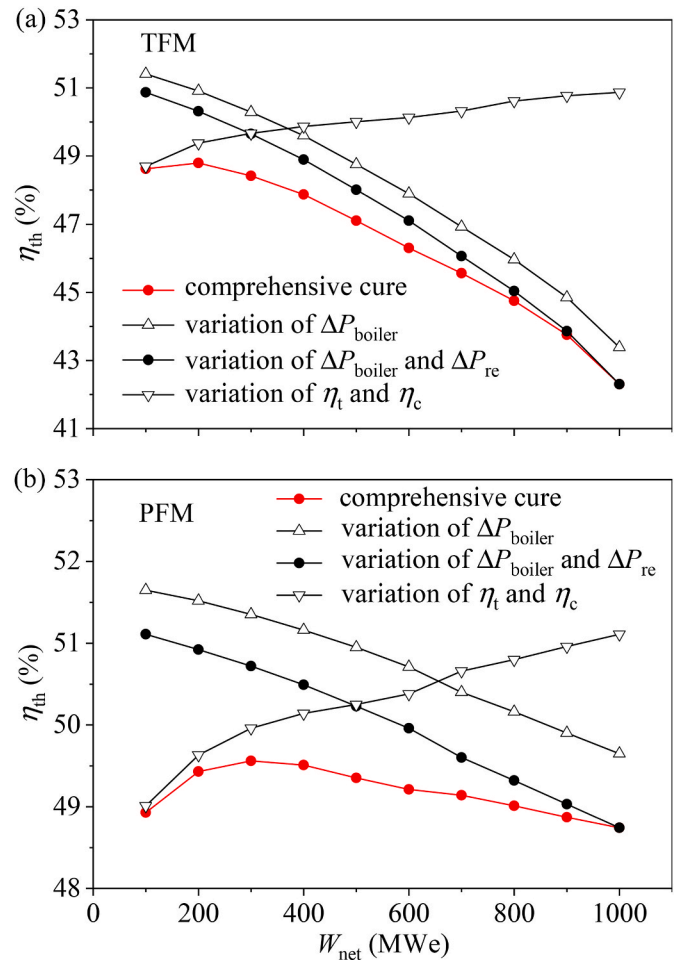


Fig. 11. Effects of pressure drops in boiler and recuperators, as well as isentropic efficiency of turbines and compressors on thermal efficiencies.

outlet and turbine T1 inlet, respectively. Ideally,  $P_2 = P_5$  yields no pressure drop in the heat exchangers between the two state points, thereby maximizing the cycle efficiency. In practice, pressure drops exist, but  $P_2 - P_5$  should be as small as possible to improve the performance of the system. Fig. 13a shows the increased  $P_2 - P_5$  versus power capacities, which are significantly larger for the TFM than for PFM, considering the logarithm coordinate used in the vertical axis of Fig. 13a.

Because the compressors supply the pressure head to circulate sCO<sub>2</sub> in the cycle, the pressure drop  $P_2 - P_5$  generates an additional load for the compressors. For the sCO<sub>2</sub> cycle, the consumption work of the compressors is larger, which is distinct from the water-steam Rankine cycle (Zhou et al., 2020). In Fig. 13b,  $W_{C1}/W_{\text{net}}$  and  $W_{C2}/W_{\text{net}}$  quantify the compression work per unit power capacity, which is also called the specific consumption work, for C1 and C2, respectively. Fig. 13b shows that the slopes of the  $W_{C1}/W_{\text{net}}$  and  $W_{C2}/W_{\text{net}}$  curves are mild with respect to  $W_{\text{net}}$  when using the PFM. That is, the specific consumption work of the two compressors was insensitive to variations in  $W_{\text{net}}$ .  $W_{C1}/W_{\text{net}}$  and  $W_{C2}/W_{\text{net}}$  achieve values of 0.21 and 0.26, respectively, at  $W_{\text{net}} = 1000$  MWe. In contrast, the specific consumption work sharply increases with an increase in  $W_{\text{net}}$  when using the TFM;  $W_{C1}/W_{\text{net}}$  and  $W_{C2}/W_{\text{net}}$  reach 0.33 and 0.35, respectively, at  $W_{\text{net}} = 1000$  MWe.

##### 4.2.2. Pressure drop in recuperators

Given that the minute nature of the channels (millimeter scale) used in the PCHE, neglecting pressure drops in the PCHE may overestimate the thermal efficiency of the system. For the parallel connection of the

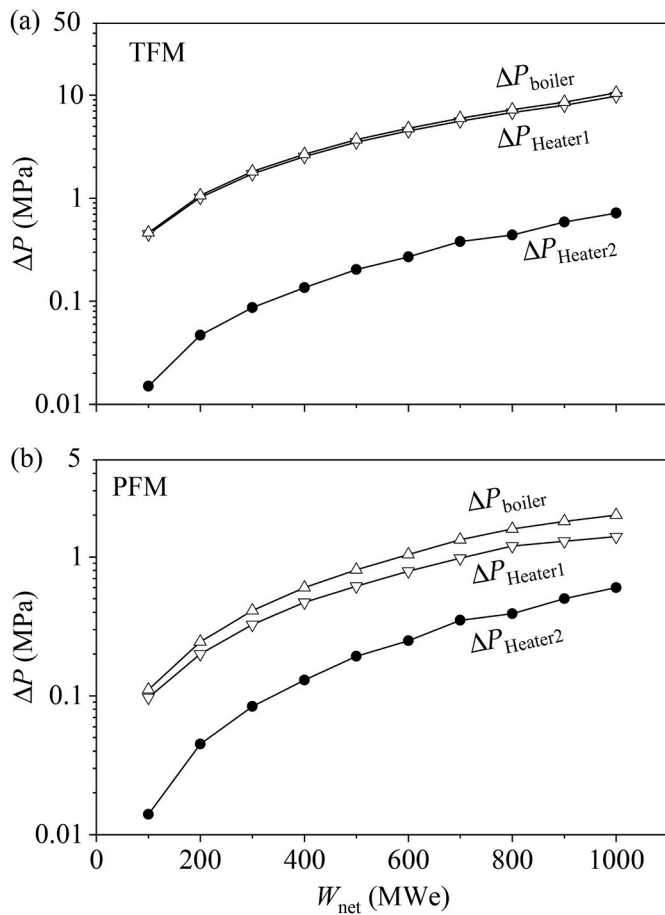


Fig. 12. Pressure drops in boiler at different power capacities.

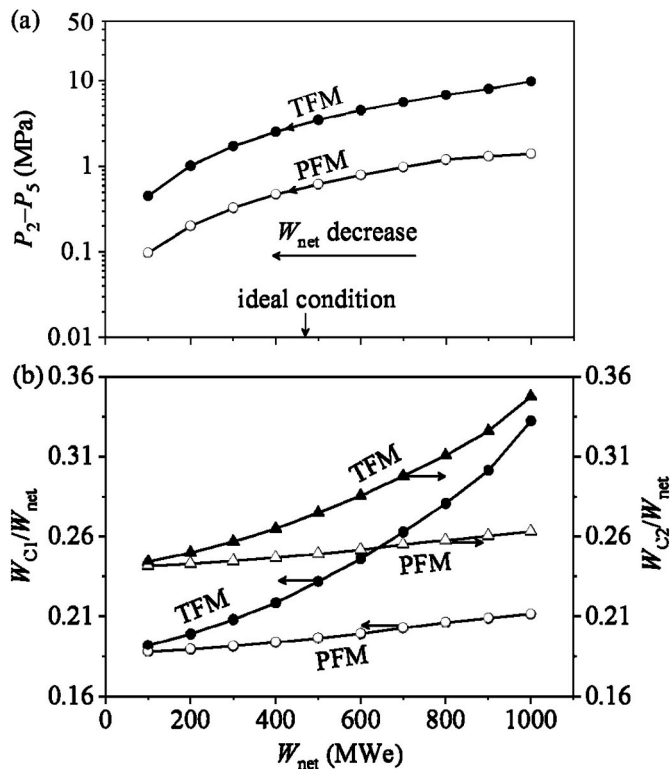


Fig. 13. Pressure drops in boiler (a) and work consumption of compressors (b).

PCHE units, the pressure drop of the entire integration package depends on the number of PCHE units, as listed in Table 10; the number of PCHE units increases with an increase in the power capacity for both HTR and LTR. Fig. 14a and b illustrates the increased pressure drops in the HTR and LTR, respectively, when the power capacity increases, which are similar to those for the sCO<sub>2</sub> boiler shown in Fig. 12.

Using the logarithmic coordinate in the vertical axis in Fig. 14c,  $\Delta P_{re}/\Delta P_{boiler}$  quantifies the relative magnitude of pressure drop in recuperators including HTR and LTR with respect to that in boiler including all the heater modules. Due to smaller pressure drop in sCO<sub>2</sub> boiler using PFM than that using TFM, the curve of  $\Delta P_{re}/\Delta P_{boiler}$  for PFM is above that for TFM. Because the PFM is recommended for practical applications, attention should be paid to the curve while using it. The  $\Delta P_{re}/\Delta P_{boiler}$  shows a decreasing trend versus  $W_{net}$ , with  $\Delta P_{re}/\Delta P_{boiler} \approx 1$  taking place at  $W_{net} = 400$  MWe. That is, the pressure drop in the recuperators is larger than that in the sCO<sub>2</sub> boiler for power capacities less than 400 MWe, but smaller than that in the sCO<sub>2</sub> boiler for power capacities greater than 400 MWe. This implies that neglecting the pressure drop in the recuperators or fixing the pressure drop to a small value (Li et al., 2019a; Mecheri and Moulec, 2016) may overestimate the overall system performance.

### 4.3. Isentropic efficiencies of turbine and compressor at various power capacities

Under ideal conditions, the expansion process of the turbine and compression process of the compressor are isentropic with no irreversible losses. However, under practical conditions, it is not feasible to convert thermal energy into mechanical work with a conversion efficiency of 100%. Fig. 15a shows the isentropic efficiencies of the turbines versus the power capacities. The horizontal axis represents power generated by the turbine. For a 1000 MWe power plant, each turbine contributes approximately 750 MWe of power. The low pressure turbine T2 and high pressure turbine T1 show similar trend for efficiencies, ranging from 88.5% at  $W_T = 73.3$  MWe to 92.3% at  $W_T = 754.8$  MWe for T2 and 85.8% at  $W_T = 72.4$  MWe to 91.3% at  $W_T = 720.8$  MWe for T1. The isentropic efficiency  $\eta_t$  is small at  $W_T = 75$  MWe; however, it increases quickly with increasing  $W_T$ ; the curve slope becomes smaller for  $W_T > 300$  MWe. T1 had a lower efficiency than T2 owing to the pressure effect. The irreversibility of a turbine can be represented in a  $T$ - $s$  diagram. As shown in Figs. 15b, 4-5 and 4'-5' represent the heat absorption process in Heaters 1 and Heater 2, respectively; 5-4' and 5'-6 represent the expansion in T1 and T2, respectively; the red line represents the case of  $W_{net} = 100$  MWe, and the black line represents the case of  $W_{net} = 1000$  MWe. For T1, the entropy increase in the expansion with  $W_{net} = 100$  MWe was greater than that with  $W_{net} = 1000$  MWe. The difference in the entropy increase at the two power capacities is indicated by  $\Delta s_{T1}$ . A similar trend was observed for T2, with a difference in the entropy increase at  $W_{net} = 100$  MWe and 1000 MWe, marked by  $\Delta s_{T2}$ . Thus, it can be concluded that the small-scale turbines exhibit higher irreversibility, yielding low efficiency.

Table 10  
The number of the PCHE parallel branches at different power capacities.

$W_{net}/\text{MWe}$	TFM		PFM	
	HTR	LTR	HTR	LTR
100	3	3	3	3
200	5	5	5	5
300	8	7	8	7
400	10	9	10	9
500	13	11	12	10
600	16	14	15	12
700	19	17	17	15
800	22	20	19	17
900	24	23	22	19
1000	29	26	24	21

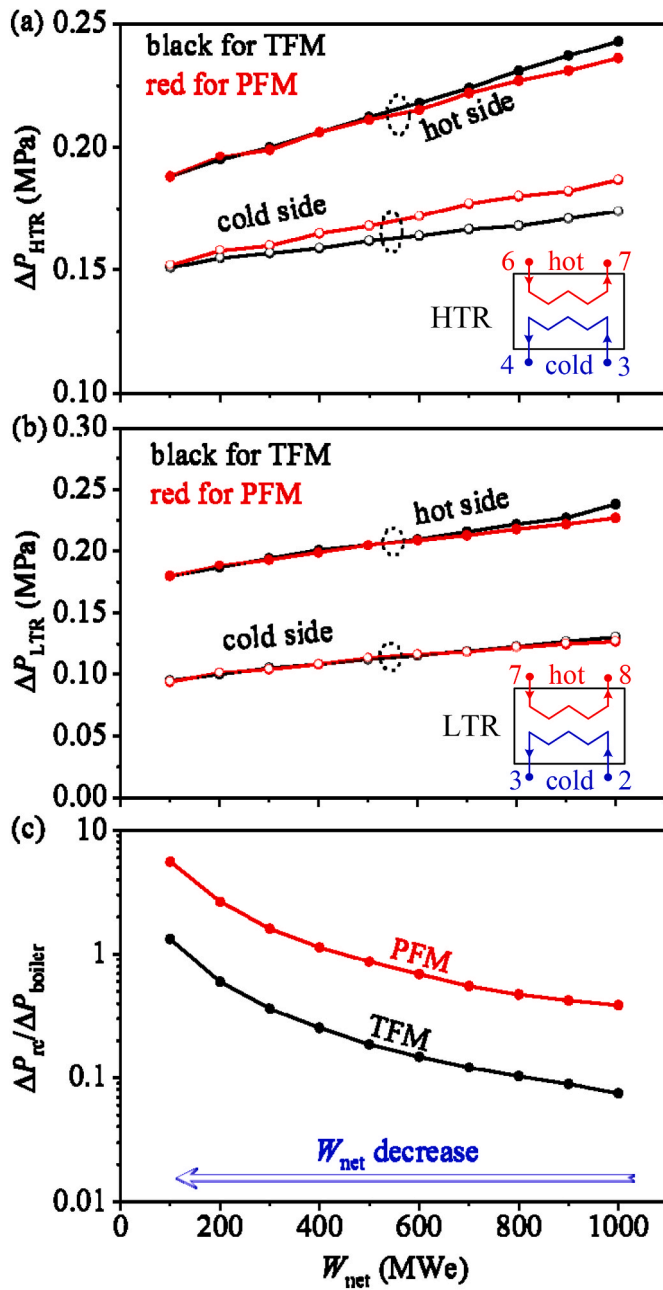


Fig. 14. Pressure drops in recuperators at different power capacities. (a) pressure drops in HTR, (b) pressure drops in LTR, (c) ratio of pressure drop in recuperators with respect to that in boiler.

Fig. 16a shows the isentropic efficiencies of the compressors versus the power capacities; the horizontal axis represents power consumption of the compressor. For a 1000 MWe power plant, the main compressor C1 consumes approximately 250 MWe of power, and the auxiliary compressor C2 consumes approximately 250 MWe of power. C1 and C2 show similar trend for efficiencies, ranging from 84.0% at  $W_T = 20.1$  MWe to 84.8% at  $W_T = 192.4$  MWe for C1 and 87.2% at  $W_T = 27.2$  MWe to 88.4% at  $W_T = 247.9$  MWe for C2. However, the curve slope of the compressors is smaller than that of the turbines. Similar to turbines, the irreversibility of a compressor can be represented in a  $T$ - $s$  diagram. In Fig. 16b, 8-1 represent the heat rejection process in the cooler; 1-2 and 8-3 represent the compression in C1 and C2, respectively, with the red line representing the case of  $W_{net} = 100$  MWe and black line representing the case of  $W_{net} = 1000$  MWe. For C1, the entropy increase in the expansion with  $W_{net} = 100$  MWe was greater than that with  $W_{net} = 1000$

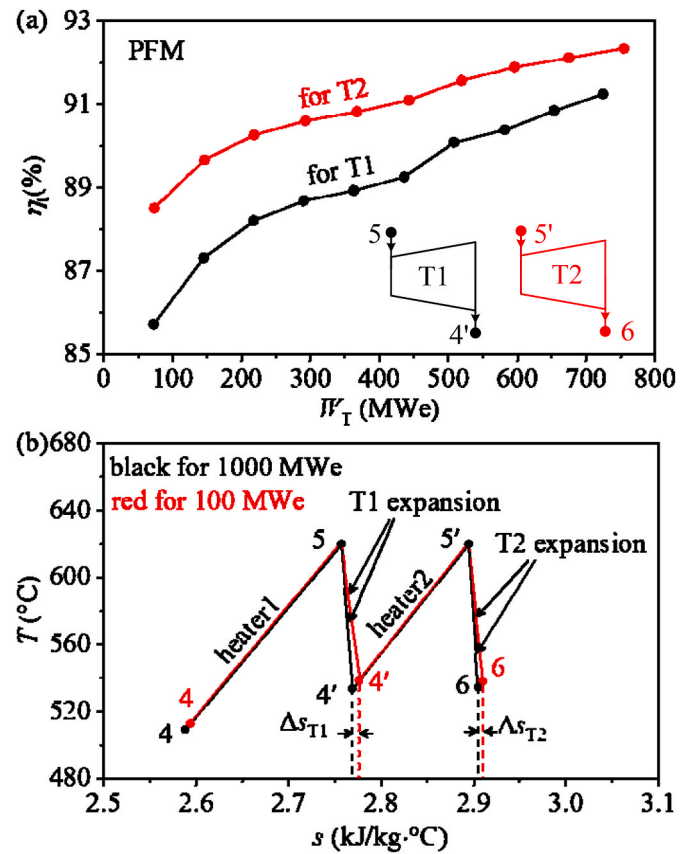


Fig. 15. Isentropic efficiencies of turbines at different power capacities (a) and  $T$ - $s$  roadmaps for heat absorption and expansion processes for  $W_{net} = 100$  MWe and 1000 MWe (b).

MWe. The difference in the entropy increase at the two power capacities is indicated by  $\Delta s_{C1}$ . A similar trend was observed for C2, with a difference in the entropy increase at  $W_{net}$  of 100 MWe and 1000 MWe, marked by  $\Delta s_{C2}$ . Small-scale compressors have a higher irreversibility, yielding low efficiency.

In Fig. 17a and b,  $I_T/W_{net}$  and  $I_C/W_{net}$  quantify the exergy loss per unit power capacity of the turbine and compressor, respectively, which is also called the specific exergy loss. Both parameters decrease as  $W_{net}$  increases; however, the  $I_C/W_{net}$  curves are mild compared with  $I_T/W_{net}$  curves.  $I_T/W_{net}$  achieved 0.045 at  $W_{net} = 100$  MWe and 0.025 at  $W_T = 1000$  MWe for T1, and  $I_C/W_{net}$  achieved 0.028 at  $W_{net} = 100$  MWe and 0.024 at  $W_{net} = 1000$  MWe for C1.

#### 4.4. Exergy loss analysis at various power capacities

This section presents the analysis of the exergy loss distribution of the components at various power capacities. Considering the power capacities of 1000 MWe and 100 MWe as representative examples, the distribution of the exergy loss proportions for each component is presented in Fig. 18, where red and black lines denote 1000 MWe and 100 MWe, respectively. The boiler contributed significantly to the total exergy loss, accounting for a large portion of the overall loss. Owing to the large pressure drop in the boiler at a large capacity, the proportion of exergy loss in the boiler at a large capacity exceeded that at a small capacity. For PFM, it accounts for 76.73% at  $W_{net} = 1000$  MWe and more than 74.99% at  $W_{net} = 100$  MWe; the proportion difference increases for TFM. For the turbine, the variation trend of the exergy loss at different power capacities differed from that of the boiler. For PFM, the proportion of exergy loss in turbine accounts for 3.97% at  $W_{net} = 1000$  MWe and less than 6.59% at  $W_{net} = 100$  MWe. For the other

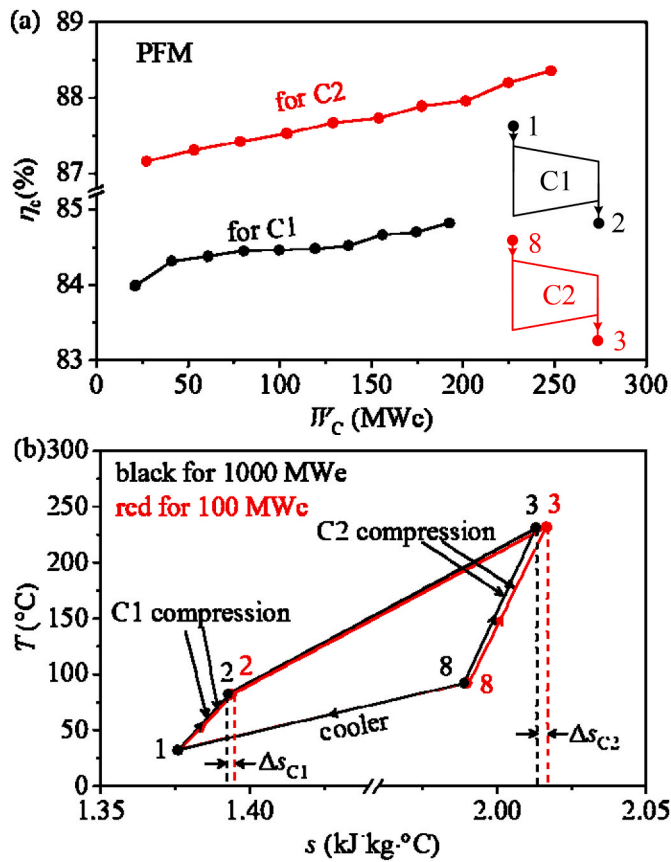


Fig. 16. Isentropic efficiencies of compressors at different power capacities (a) and  $T$ - $s$  roadmaps for heat rejection and compression processes for  $W_{\text{net}} = 100$  MWe and 1000 MWe (b).

components, the exergy destruction distributions versus power capacities were similar. Furthermore, to compare the relative magnitudes of the total irreversibility losses at different capacities, a dimensionless ratio of the total irreversibility losses to the net power output was defined and denoted as  $I_{\text{total}}/W_{\text{net}}$ . This ratio represents the irreversible losses per unit of net power output. Fig. 19 plots the curves of  $I_{\text{total}}/W_{\text{net}}$  at various power capacities, showing an opposite trend to that of the thermal efficiencies at various power capacities, as shown in Fig. 10a;  $I_{\text{total}}/W_{\text{net}}$  first decreases and then increases with increasing power capacity. For the PFM, 300 MWe corresponded to the minimum relative exergy destruction, whereas it was 200 MWe for the TFM.

##### 5. Comments on thermal efficiencies at different power capacities

Recently, scale laws have been developed to explore the system performance at different power capacities of  $\text{sCO}_2$  coal-fired power systems (Liu et al., 2020c). The laws focused on the effect of the pressure drops in the  $\text{sCO}_2$  boiler on the system performance by neglecting the pressure drops in the heat exchangers, except for the  $\text{sCO}_2$  boiler, and by assuming a constant isentropic efficiency of the turbomachinery. The thermal efficiency of the system was found to decrease with the increase in the power capacity (Liu et al., 2020c).

In contrast to Ref. (Liu et al., 2020c), the  $\text{sCO}_2$  cycle was coupled with models of various components, including  $\text{sCO}_2$  boilers, recuperator heat exchangers, turbines, and compressors in the present study. Because the heat recovery of the cycle is three to four times the net power output (Xu et al., 2018) and the thermal load for a single recuperator is limited, a fluid network was proposed for the first time to integrate recuperator units. A model was established for both a single

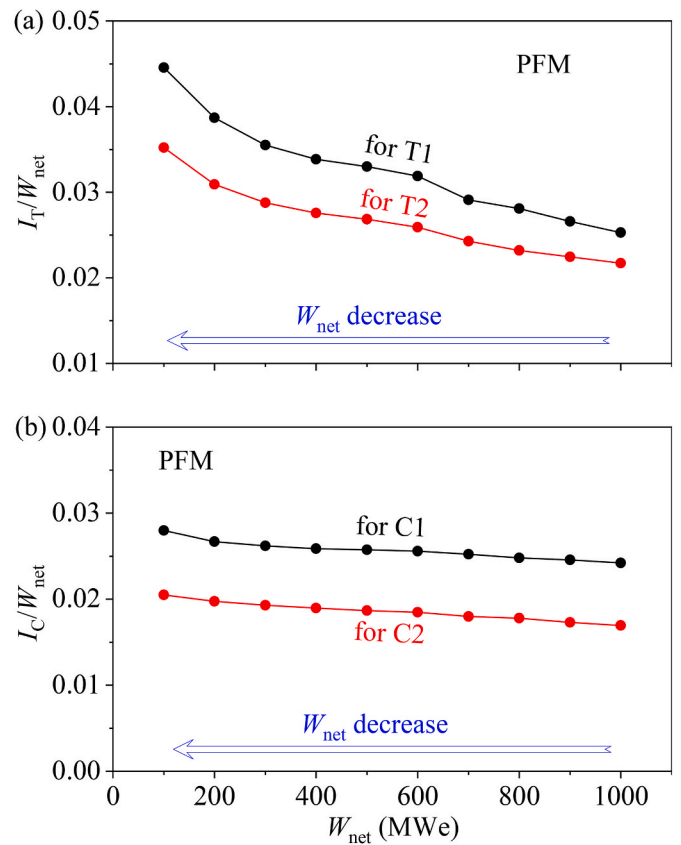


Fig. 17. Exergy loss of turbines and compressors per unit power capacity (a) Turbines (b) Compressors.

recuperator unit and the entire integration package. The proposed model also dealt with varied efficiencies at different power capacities. To eliminate the penalty effect of ultra-large pressure drops in the  $\text{sCO}_2$  boiler, the PFM was applied and compared with the TFM. We believe that the results based on the current model are closer to practical scenarios than those of our previous study (Liu et al., 2020c) and other related studies, which fixed the pressure drops in the recuperators and isentropic efficiencies of turbomachinery in their cycle analyses (Moulicc, 2013; Li et al., 2019a; Mecheri and Moulicc, 2016; Park et al., 2018; Wang et al., 2018; Zhou et al., 2020).

A parabolic distribution is identified for thermal efficiencies versus power capacities, which is the outcome of the deteriorated performance owing to pressure drops in the heat exchangers and the improved efficiencies of turbomachinery. When  $W_{\text{net}}$  is increased from 100 MWe to 1000 MWe, the thermal efficiencies of the system increase, reach a maximum, and then decrease, which differs from the decreased thermal efficiencies when considering the pressure drops in  $\text{sCO}_2$  boilers only (Liu et al., 2020c).

Economy, in addition to plant efficiency, is a critical aspect to enhance market competitiveness of the  $\text{sCO}_2$  power plant and accelerates its commercialization. The recuperator is recognized as a key technology in the development of the  $\text{sCO}_2$  cycle. Because the heat recovery reaches three to four times the net power output of  $\text{sCO}_2$  cycle, the cost of  $\text{sCO}_2$  recuperator dominates the total component cost of coal-fired  $\text{sCO}_2$  power plant. The selection of pinch temperature  $\Delta T$  influences the cycle performance; too small a value of pinch temperature significantly increases the cost of heat exchangers owing to the increase of volume and fabrication difficulty, whereas too large a value of pinch temperature deteriorates the cycle efficiency, which further increases the coal consumption of the power plant and operating costs. As shown in Fig. 20, both the cost of the recuperator and thermal efficiency decrease as the pinch temperature  $\Delta T$  increases. For the capacity of 1000

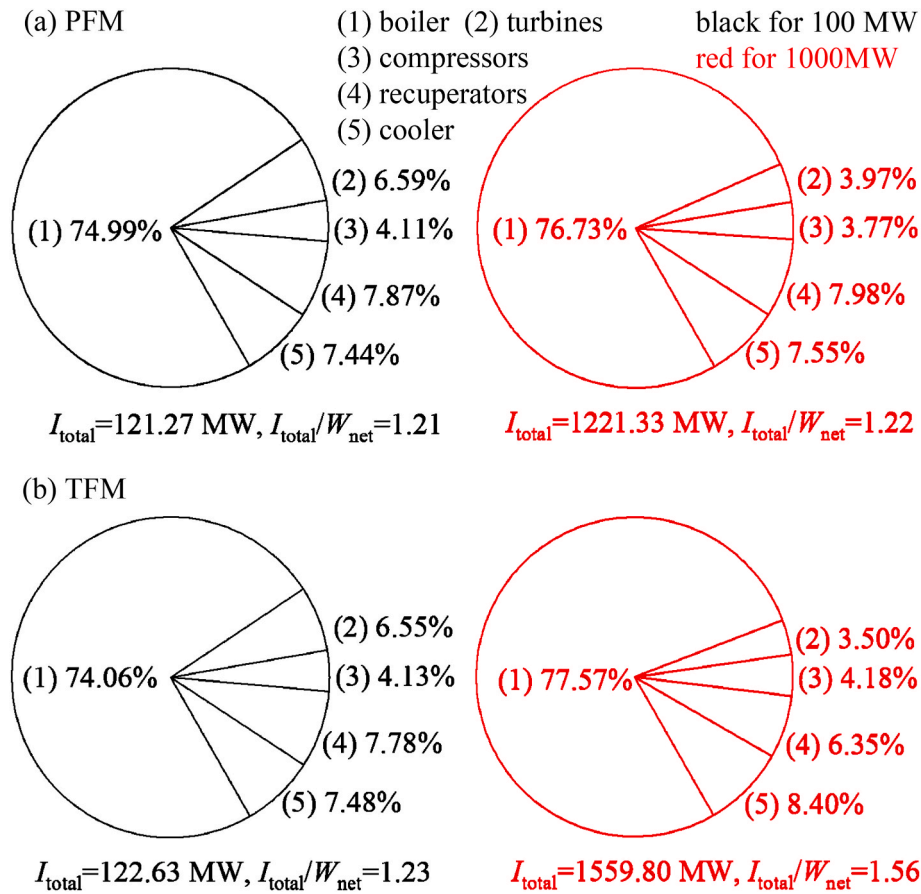


Fig. 18. Exergy destruction distributions in the cycle at power capacities of 1000 MWe and 100 MWe.

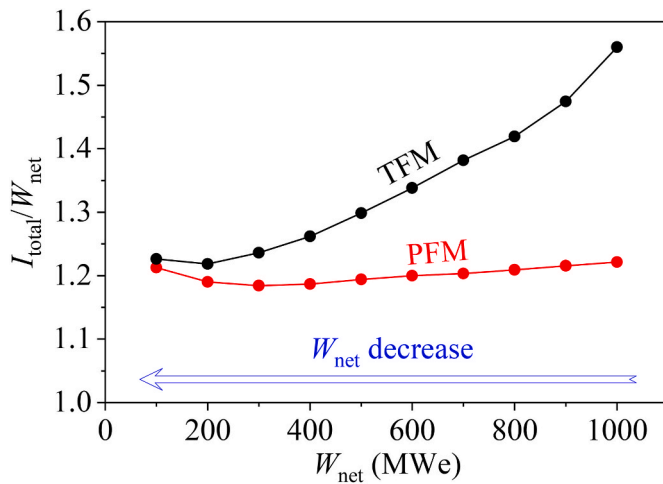


Fig. 19. The ratio of the total exergy destruction to power capacities.

MWe, the cost of recuperator is 172.6 M\$ when the pinch temperature is 10 °C, accounting for 44.02% of the total component cost, and the thermal efficiency is as high as 53.6% at  $\Delta T = 10$  °C. When the pinch temperature is raised to 30 °C, the cost of recuperator is reduced to approximately 86.0 M\$ and thermal efficiency is lowered to 49.2%.

An economic comparison between a coal-fired sCO<sub>2</sub> power plant and water-steam power plant at  $W_{net} = 1000$  MWe was presented in our previous study (Xu et al., 2021). Compared with the water-steam system, the cost of the sCO<sub>2</sub> turbine decreased by 30.0% owing to the compact size, and the cost of sCO<sub>2</sub> boiler increased by 36.3% due to the

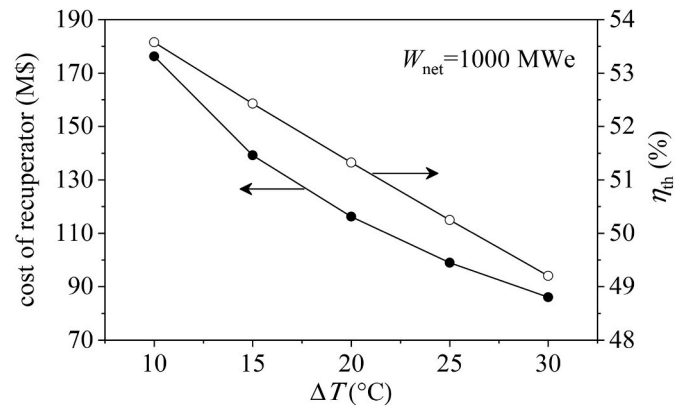


Fig. 20. Effect of pinch temperature in recuperator on the cost of recuperator and thermal efficiency.

increase in the grade and thickness of heating surface steel. The cost of sCO<sub>2</sub> recuperator is one order of magnitude higher than that of a water-steam power plant. Therefore, the entire sCO<sub>2</sub> power system increases the total equipment cost by 1.92 times. However, owing to the superiority in efficiency of sCO<sub>2</sub> power plant over the 30-year lifespan of the power plant, the levelized cost of electricity (LCOE) is 60.56 \$/MWh, which is 1.32% lower compared with that of the water-steam system. Therefore, we conclude that, even though the fabrication cost increases, the sCO<sub>2</sub> power system is preferable over the water-steam system. The cost of the sCO<sub>2</sub> power system can be further reduced by optimizing the recuperator, which is a key component of the system.

Moreover, according to the cost model, the cost of the entire sCO<sub>2</sub>



power system is approximately proportional to the net output power  $W_{\text{net}}$ . However, as the power capacity was increased from 100 MWe to 1000 MWe, the thermal efficiencies increased, reached a maximum, and then decreased. The maximum thermal efficiency occurred at  $W_{\text{net}} = 300$  MWe when the PFM was used; therefore, the economy at  $W_{\text{net}} = 300$  MWe was optimal.

## 6. Conclusions

A comprehensive model was introduced by incorporating various component models. Owing to the limited load of a single recuperator heat exchanger, a fluid network integrating recuperator units was established for large-scale heat recovery. A thermal-hydraulic model was proposed for both the single units and the integration package. For the sCO<sub>2</sub> boiler, the total thermal load was assigned to the various heaters. Owing to the strong penalty effect of the pressure drop, comparative studies were performed for the sCO<sub>2</sub> boiler using the TFM and PFM. For axial-flow turbomachinery, various losses were considered to predict the efficiencies at different power capacities. Ten power capacities ranging from 100 MWe to 1000 MWe were investigated. As the power capacity increased, the pressure drops in the boiler and recuperator increased. Compared with the pressure drop in the boiler, the pressure drop in the recuperator was smaller, ranging from 0.10 MPa to 0.25 MPa. Therefore, the pressure drop in sCO<sub>2</sub> boiler exhibits a dominant contribution to the total pressure drop. The pressure drops in the sCO<sub>2</sub> boiler and recuperator should be overcome via compressors by incorporating an additional load to increase the specific consumption work, which deteriorates the system performance. The penalty effect of pressure drops is significantly relieved by using the PFM, for which the sCO<sub>2</sub> boiler is subdivided into several heater modules using a reduced flow rate and shorter length for each module compared with the PFM.

For axial-flow turbomachinery, as the power capacity increases, the irreversible losses decrease, resulting in a higher isentropic efficiency. The thermal efficiency of the system is a tradeoff between the deteriorated performance owing to pressure drops in heat exchangers and the improved performance owing to increased turbomachinery efficiency at larger power capacities. As the power capacity was increased from 100 MWe to 1000 MWe, the thermal efficiencies increased, reached a maximum, and then decreased. The maximum efficiency occurred at  $W_{\text{net}}$  of 300 MWe and 200 MWe with the PFM and TFM, respectively. This study provides insights for the selection of the optimal power capacity of the sCO<sub>2</sub> coal-fired power plants.

## CRedit authorship contribution statement

**Zhaofu Wang:** Methodology, Software, Investigation, Writing – original draft. **Jinliang Xu:** Conceptualization, Supervision, Funding acquisition, Writing – review & editing. **Tianze Wang:** Software, Methodology. **Zheng Miao:** Conceptualization, Methodology. **Qinyang Wang:** Writing – review & editing. **Guanglin Liu:** Formal analysis.

## Declaration of competing interest

The authors declare that they have no known competing financial interests or personal relationships that could have appeared to influence the work reported in this paper.

## Data availability

Data will be made available on request.

## Acknowledgements

This work was supported by Natural Science Foundation of China (52130608, 51821004).

## References

- Ainley, D.G., Mathieson, G.C.R., 1951. A Method of Performance Estimation for Axial-Flow Turbines. ARC Technical Report.
- Aungier, R.H., 2003. Axial-flow Compressors: A Strategy for Aerodynamic Design and Analysis. ASME Press, New York, USA.
- Aungier, R.H., 2005. Turbine Aerodynamics: Axial-Flow and Radial-Inflow Turbine Design and Analysis. ASME Press, New York, USA.
- Bidkar, R.A., Mann, A., Singh, R., Sevincer, E., Cich, S., Day, M., 2016. Conceptual designs of 50 MWe and 450 MWe supercritical CO<sub>2</sub> turbomachinery trains for power generation from coal. Part 1: cycle and turbine. In: The 5th Symposium Supercritical CO<sub>2</sub> Power Cycles. March, Texas, USA, pp. 28–31.
- Cho, J., Shin, H., Cho, J., Ra, H.S., Roh, C., Lee, B., Lee, G., Choi, B., Baik, Y.J., 2018. Preliminary power generating operation of the supercritical carbon dioxide power cycle experimental test loop. In: The 6th International Supercritical CO<sub>2</sub> Power Cycles Symposium. March, Pennsylvania, USA, pp. 27–29.
- Da, L.L., Manente, G., Lazzaretto, A., 2014. New efficiency charts for the optimum design of axial flow turbines for organic Rankine cycles. Energy 77, 447–459.
- Dostal, V., 2004. A Supercritical Carbon Dioxide Cycle for Next Generation Nuclear Reactors. Massachusetts Institute of Technology, Cambridge, USA.
- Dunham, J., Came, P.M., 1970. Improvements to the Ainley–Mathieson method of turbine performance prediction. J. Eng. Power 92, 252–256.
- Dyreby, J., Klein, S., Nellis, G., Reindl, D., 2014. Design considerations for supercritical carbon dioxide Brayton cycles with recompression. J. Eng. Gas Turbines Power 136 (10), 101701.
- Fan, Q., 2014. Boiler Principle. China Electric Power Press, Beijing, China.
- Fan, H., Zhang, Z., Dong, J., Xu, W., 2018. China's R&D of advanced ultra-supercritical coal fired power generation for addressing climate change. Therm. Sci. Eng. Prog. 5, 364–371.
- Fan, Y., Tang, G., Yang, D., Li, X., Wang, S., 2020. Integration of S-CO<sub>2</sub> Brayton cycle and coal-fired boiler: thermal-hydraulic analysis and design. Energy Convers. Manag. 225, 113452.
- Fleming, D., Holschuh, T., Conboy, T., Rochau, G., Fuller, R., 2012. Scaling considerations for a multi-megawatt class supercritical CO<sub>2</sub> Brayton cycle and path forward for commercialization. In: ASME, Editor. Proceedings of ASME Turbo Expo 2012: Turbine Technical Conference and Exposition. June, Copenhagen, Denmark, pp. 11–15.
- Fu, Q., 2005. Thermodynamic Analysis Method of Energy System. Xi'an Jiaotong University Press, Xi'an, Shanxi, China.
- Guo, J., Lia, M., Xu, J., Yan, J., Ma, T., 2020. Energy, exergy and economic (3E) evaluation and conceptual design of the 1000 MW coal-fired power plants integrated with S-CO<sub>2</sub> Brayton cycles. Energy Convers. Manag. 211, 112713.
- Han, W., Zhang, Y., Li, H., Yao, M., Wan, Y., Feng, Z., Zhou, D., Dan, G., 2019. Aerodynamic design of the high pressure and low pressure axial turbines for the improved coal-fired recompression sCO<sub>2</sub> reheated Brayton cycle. Energy 179, 442–453.
- Heatric, 2017. www.heatric.com accessed 17.08.15.
- Holcomb, G.R., Carney, C., Dogan, O.N., 2016. Oxidation of alloys for energy applications in supercritical CO<sub>2</sub> and H<sub>2</sub>O. Corrosion Sci. 109, 22–35.
- Jiang, Y., Liese, E., Zitney, S.E., Bhattacharyya, D., 2018a. Optimal design of microtube recuperators for an indirect supercritical carbon dioxide recompression closed Brayton cycle. Appl. Energy 216, 634–648.
- Jiang, Y., Liese, E., Zitney, S.E., Bhattacharyya, D., 2018b. Design and dynamic modeling of printed circuit heat exchangers for supercritical carbon dioxide Brayton power cycles. Appl. Energy 231, 1019–1032.
- Kacker, S.C., Okapuu, U., 1982. A mean line prediction method for axial flow turbine efficiency. J. Eng. Power 104, 111–119.
- Kim, S.G., Lee, Y., Ahn, Y., Lee, J.L., 2016. CFD aided approach to design printed circuit heat exchangers for supercritical CO<sub>2</sub> Brayton cycle application. Ann. Nucl. Energy 92, 175–185.
- Li, H., Zhang, Y., Yang, Y., Han, W., Yao, M., Bai, W., Zhang, L., 2019a. Preliminary design assessment of supercritical CO<sub>2</sub> cycle for commercial scale coal-fired power plants. Appl. Therm. Eng. 158, 113785.
- Li, H., Zhang, Y., Yao, M., Yang, Y., Han, W., Bai, W., 2019b. Design assessment of a 5 MW fossil fired supercritical CO<sub>2</sub> power cycle pilot loop. Energy 174, 792–804.
- Li, H., Fan, G., Cao, L., Yang, Y., Yan, X., Dai, Y., Zhang, G., Wang, J., 2020. A comprehensive investigation on the design and off-design performance of supercritical carbon dioxide power system based on the small-scale lead-cooled fast reactor. J. Clean. Prod. 256, 120720.
- Li, X., Tang, G., Fan, Y., Yang, D., 2022. A performance recovery coefficient for thermal-hydraulic evaluation of recuperator in supercritical carbon dioxide Brayton cycle. Energy Convers. Manag. 256, 115393.
- Linares, J.I., Arenas, E., Cantizano, A., Porras, J., Moratill, B.Y., Carmona, M., Batet, L., 2018. Sizing of a recuperative supercritical CO<sub>2</sub> Brayton cycle as power conversion system for DEMO fusion reactor based on Dual Coolant Lithium Lead blanket. Fusion Eng. Des. 134, 79–91.
- Liu, C., 2022. Research on Boiler and Recuperator in Supercritical Carbon Dioxide Coal-Fired Power Generation System. North China Electric Power University, Beijing, China.
- Liu, Z., Liu, Z., Cao, X., Luo, T., Yang, X., 2020a. Advanced exergoeconomic evaluation on supercritical carbon dioxide recompression Brayton cycle. J. Clean. Prod. 256, 120537.
- Liu, M., Yang, K., Zhang, X., Yan, J., 2020b. Design and optimization of waste heat recovery system for supercritical carbon dioxide coal-fired power plant to enhance the dust collection efficiency. J. Clean. Prod. 275, 122523.

- Liu, C., Xu, J., Li, M., Wang, Z., Xu, Z., Xie, J., 2020c. Scale law of sCO<sub>2</sub> coal fired power plants regarding system performance dependent on power capacities. *Energy Convers. Manag.* 226, 113505.
- Liu, C., Xu, J., Li, M., Wang, Q., Liu, G., 2022. The comprehensive solution to decrease cooling wall temperatures of sCO<sub>2</sub> boiler for coal fired power plant. *Energy* 252, 124021.
- Mecheri, M., Moulic, L.Y., 2016. Supercritical CO<sub>2</sub> Brayton cycles for coal-fired power plants. *Energy* 103, 758–771.
- Meng, Y., Cao, Y., Li, J., Liu, C., Li, J., Wang, Q., Cai, G., Zhao, Q., Liu, Yi, Meng, X., Ge, W., Yang, Q., 2022. The real cost of deep peak shaving for renewable energy accommodation in coal-fired power plants: calculation framework and case study in China. *J. Clean. Prod.* 367, 132913.
- Moulic, L.Y., 2013. Conceptual study of a high efficiency coal-fired power plant with CO<sub>2</sub> capture using a supercritical CO<sub>2</sub> Brayton cycle. *Energy* 49, 32–46.
- National Bureau of Statistics of China, 2020. *China Energy Statistical Yearbook*. China Statistics Press, Beijing, China.
- Park, S., Kim, J., Yoon, M., Rhim, D., Yeom, C., 2018. Thermodynamic and economic investigation of coal-fired power plant combined with various supercritical CO<sub>2</sub> Brayton power cycle. *Appl. Therm. Eng.* 130, 611–623.
- Qi, Y., Liu, T., Jing, L., 2023. China's energy transition towards carbon neutrality with minimum cost. *J. Clean. Prod.* 388, 135904.
- Qiao, Z., Cao, Y., Li, P., Wang, X., Romero, C.E., Pan, L., 2020. Thermo-economic analysis of a CO<sub>2</sub> plume geothermal and supercritical CO<sub>2</sub> Brayton combined cycle using solar energy as auxiliary heat source. *J. Clean. Prod.* 256, 120374.
- Saber, M., Commenge, J.M., Falk, L., 2009. Rapid design of channel multi-scale networks with minimum flow maldistribution. *Chem. Eng. Process* 48, 723–733.
- Sun, E., Xu, J., Li, M., Liu, G., Zhu, B., 2018. Connected-top-bottom-cycle to cascade utilize flue gas heat for supercritical carbon dioxide coal fired power plant. *Energy Convers. Manag.* 172, 138–154.
- Sun, E., Xu, J., Hu, H., Li, M., Miao, Z., Yang, Y., Liu, J., 2019. Overlap energy utilization reaches maximum efficiency for S-CO<sub>2</sub> coal fired power plant: a new principle. *Energy Convers. Manag.* 195, 99–113.
- Sun, E., Xu, J., Li, M., Li, H., Liu, C., Xie, J., 2020. Synergetics: the cooperative phenomenon in multi-compressions S-CO<sub>2</sub> power cycles. *Energy Convers. Manag.* X 7, 100042.
- Thimsen, D., Weitzel, P., 2016. Challenges in designing fuel-fired sCO<sub>2</sub> heaters for closed sCO<sub>2</sub> Brayton cycle power plants. In: 5th International Supercritical CO<sub>2</sub> Power Cycles Symposium. March, San Antonio, Texas, USA, pp. 29–31.
- Wang, Y., Guenette, G., Hejzlar, P., Driscoll, M., 2004. Compressor design for the supercritical CO<sub>2</sub> Brayton cycle. In: 2nd International Energy Conversion Engineering Conference. Providence, Rhode Island, USA, 16–19, August.
- Wang, Z., Sun, B., Wang, J., Hou, L., 2014. Experimental study on the friction coefficient of supercritical carbon dioxide in pipes. *Int. J. Greenh. Gas Control* 25, 151–161.
- Wang, F., Su, H., Chen, T., Yu, Q., Huang, Y., Zhang, Y., Shen, T., 2018. Coupled modeling of combustion and hydrodynamics for a supercritical CO<sub>2</sub> boiler. *Appl. Therm. Eng.* 143, 711–718.
- Wang, Z., Sun, E., Xu, J., Liu, C., Liu, G., 2021a. Effect of flue gas cooler and overlap energy utilization on supercritical carbon dioxide coal fired power plant. *Energy Convers. Manag.* 249, 114866.
- Wang, Q., Ma, X., Xu, J., Li, M., Wang, Y., 2021b. The three-regime-model for pseudo-boiling in supercritical pressure. *Int. J. Heat Mass Tran.* 181, 121875.
- Wang, Z., Zheng, H., Xu, J., Li, M., Sun, E., Guo, Y., Liu, C., Liu, G., 2022. The roadmap towards the efficiency limit for supercritical carbon dioxide coal fired power plant. *Energy Convers. Manag.* 269, 116166.
- Wang, T., Xu, J., Wang, Z., Zheng, H., Qi, J., Liu, G., 2023. Irreversible losses, characteristic sizes and efficiencies of sCO<sub>2</sub> axial turbines dependent on power capacities. *Energy* 275, 127437.
- Xie, B., Zhang, R., Chen, X., 2023. China's optimal development pathway of intermittent renewable power towards carbon neutrality. *J. Clean. Prod.* 406, 136903.
- Xu, J., Sun, E., Li, M., Liu, H., Zhu, B., 2018. Key issues and solution strategies for supercritical carbon dioxide coal fired power plant. *Energy* 157, 227–246.
- Xu, J., Liu, C., Sun, E., Xie, J., Li, M., Yang, Y., Liu, J., 2019. Perspective of S-CO<sub>2</sub> power cycles. *Energy* 186, 115831.
- Xu, G., Schwarz, P., Yang, H., 2020. Adjusting energy consumption structure to achieve China's CO<sub>2</sub> emissions peak. *Renew. Sustain. Energy Rev.* 122, 109737.
- Xu, J., Wang, X., Sun, E., Li, M., 2021. Economic comparison between sCO<sub>2</sub> power cycle and water-steam Rankine cycle for coal-fired power generation system. *Energy Convers. Manag.* 238, 114150.
- Yang, D., Tang, G., Fan, Y., Li, X., Wang, S., 2020. Arrangement and three-dimensional analysis of cooling wall in 1000 MW S-CO<sub>2</sub> coal-fired boiler. *Energy* 197, 117168.
- Zhou, J., Zhu, M., Xu, K., Su, S., Tang, Y., 2020. Key issues and innovative double-tangential circular boiler configurations for the 1000 MW coal-fired supercritical carbon dioxide power plant. *Energy* 199, 117474.
- Zhu, B., Xu, J., Wu, X., Xie, J., Li, M., 2019. Supercritical “boiling” number, a new parameter to distinguish two regimes of carbon dioxide heat transfer in tubes. *Int. J. Therm. Sci.* 136, 254–266.
- Zhu, B., Xu, J., Yan, C., Xie, J., 2020. The general supercritical heat transfer correlation for vertical up-flow tubes: K number correlation. *Int. J. Heat Mass Tran.* 148, 119080.
- d*: diameter, m  
*e*: exergy per unit mass, kJ/kg  
*E*: exergy, kJ  
*f*: friction coefficient  
*G*: mass flux, kg/m<sup>2</sup>s  
*h*: enthalpy, kJ/kg heat transfer coefficients, W/(m<sup>2</sup>K)  
*I*: exergy destruction, MW  
*k*: thermal conductivity of metal wall, W/(mK)  
*L*: length of PCHE, m  
*l<sub>w</sub>*: wave length of PCHE, m  
*M*: mass flow rate in main-pipe, kg/s  
*m*: mass flow rate of CO<sub>2</sub>, kg/s mass flow rate in branch-pipe, kg/s  
*N*: number of parallel branches  
*N<sub>c</sub>*: number of PCHE cold plates  
*N<sub>h</sub>*: number of PCHE hot plates  
*N<sub>s</sub>*: specific speed of turbomachinery  
*Nu*: Nusselt number  
*n*: rotating speed of turbomachinery, r/min  
*P*: pressure, MPa  
*q*: heat flux, kW/m<sup>2</sup>  
*Q*: thermal load, MW; heating value, kJ/kg volume flow rate in turbomachinery, m<sup>3</sup>/s  
*R*: degree of reaction in turbomachinery  
*R<sub>p</sub>*: the ratio of the number of hot plates *N<sub>h</sub>* with respect to the cold plates *N<sub>c</sub>*  
*Re*: Reynolds number  
*S*: heat transfer area of total heaters below the furnace exit  
*s*: entropy, kJ/kg  
*T*: temperature, °C  
*T'*: flue gas temperature at furnace outlet, °C  
*t<sub>1</sub>*: edge width of PCHE, mm  
*t<sub>2</sub>*: wall thickness of PCHE, mm  
*t<sub>3</sub>*: ridge width of PCHE, mm  
*t<sub>e</sub>*: equivalent wall thickness, mm  
*U*: peripheral velocity of rotor, m/s  
*U<sub>k</sub>*: overall heat transfer coefficient of kth sub-exchanger, W/(m<sup>2</sup>K)  
*V*: absolute velocity in turbomachinery, m/s  
*V<sub>x</sub>*: meridional velocity in turbomachinery, m/s  
*(VC)<sub>m</sub>*: average specific heat of flue gas, kJ/(kgK)  
*W*: output/ input work, MW relative velocity in turbomachinery, m/s  
*x*: split ratio

### Greek symbols

- α*: wave angle of PCHE wave channel, ° absolute flow angle in turbomachinery, °  
*β*: relative flow angle in turbomachinery  
*φ*: boiler heat retention coefficient flow coefficient of turbomachinery  
*ψ*: loading coefficient of turbomachinery  
*Δ*: difference; absolute roughness of tubes, mm  
*ΔP*: pressure drop, MPa  
*η*: efficiency  
*ρ*: density, kg/m<sup>3</sup>  
*θ'*: dimensionless flue gas temperature at furnace outlet  
*ε<sup>ym</sup>*: furnace emissivity

### Subscripts

- 1, 2, 3 ...: state points  
*a*: acceleration  
*ar*: received basis of the designed coal  
*ave*: average  
*c*: cold temperature side  
*cal*: calculated value  
*ex*: exhaust flue gas  
*f*: fluid; friction  
*g*: gravity gravitational acceleration  
*fg,i*: interface of high temperature flue gas and moderate temperature flue gas  
*fg,o*: interface of moderate temperature flue gas and low temperature flue gas  
*fg,ex*: interface of exhaust flue gas  
*flame*: theoretical combustion  
*h*: high temperature side  
*i*: inner of tube; inlet of moderate temperature flue gas region; ith PCHE branches  
*k*: the kth sub-exchanger of recuperators  
*net*: net power out put  
*o*: outer of tube; outlet of moderate temperature flue gas region  
*T*: turbine  
*th*: thermal adiabatic combustion  
*x*: x axis  
*y*: y axis  
*z*: z axis

### Abbreviation

- AP: air preheater  
 C1: the main compressor  
 C2: the auxiliary compressor  
 EAP: external air preheater  
 HRH: high temperature reheater

### Glossary

- A<sub>k</sub>*: heat transfer area of cold side for kth sub-exchanger  
*B<sub>cal</sub>*: coal consumption rate, kg/s  
*B<sub>o</sub>*: Boltzmann constant

*HTR*: high-temperature recuperator  
*LMTD*: logarithmic mean temperature difference  
*LHV*: lower heating value  
*LRH*: low temperature reheater  
*LTR*: low-temperature recuperator  
*PFM*: partial flow mode  
*R*: rotor  
*RC*: recompression cycle

*RH*: reheating  
*OEU*: overlap energy utilization  
*S*: stator  
*SC*: simple cycle  
*SH*: superheater  
*T1, T2*: turbine  
*TFM*: total flow mode